

Journal of Sedimentary Research

EPISODIC POSTGLACIAL DELTAIC PULSES IN THE GULF OF CADIZ: IMPLICATIONS FOR THE DEVELOPMENT OF A TRANSGRESSIVE SHELF AND DRIVING ENVIRONMENTAL CONDITIONS

--Manuscript Draft--

Manuscript Number:	2021.110R3
Article Type:	Research Article
Corresponding Author:	Álvaro Carrión-Torrente Instituto Andaluz de Ciencias de la Tierra Armillá, Granada SPAIN
First Author:	Álvaro Carrión-Torrente
Order of Authors:	Álvaro Carrión-Torrente Francisco José Lobo Ángel Puga-Bernabéu Isabel Mendes Susana Lebreiro Marga García David Van Rooij María Luján María Isabel Reguera Laura Antón
Abstract:	<p>The postglacial sea-level rise after the Last Glacial Maximum provided ideal conditions to study the transgressive sedimentary response to sudden shelf flooding driven by different rates of sea-level rise. In this study, a high-resolution seismic stratigraphic interpretation and sedimentological analysis were conducted on data from the northern Gulf of Cadiz continental shelf (SW Iberian Peninsula), in order to: (1) understand the succession of sedimentary processes during each shelf flooding episode; (2) explore the significance of variable rates of sea-level rise, sediment fluxes and climatic conditions on the development of postglacial deposits.</p> <p>Four backstepping seismic postglacial transgressive units (PTUs; 4 to 1 from oldest to youngest) that are linked to the retreating mouth of the Guadiana River were interpreted. Together, these seismic units display a wedge-shape geometry, are located over the inner to middle shelf, and overlie a regional unconformity formed during the Last Glacial Maximum. Each PTU can be divided into several sub-units with distinctive seismic facies that have a similar stratigraphic organization. Each PTU contains lower sub-units that are composed of low-angle tangential oblique clinofolds. The clinofolds are locally topped by a channelized sub-unit. The distal and/or lateral parts of the clinofolds are occasionally buried by sheet-like semi-transparent subunits. The uppermost sub-units are present over the proximal and central parts of each seismic unit and are also sheet-like. PTU's can also be subdivided and described sedimentologically. Fine-grained sands with intercalated silty layers dominate the lower part of each PTU (lower clinofold sub-units). The upper part of each PTU (upper sheet-like sub-units) is characterised by reworked facies, composed of highly fragmented bioclasts within a mixture of silt and coarse to medium sand. Finally, mud deposits occur as a sediment drape over the PTUs.</p> <p>The internal structure of each PTU reveals several phases of development under a general process of transgressive submergence in which both coastal and marine deposits were formed and eventually preserved. The initial phase involved the development of coarse-grained deltas in shallow water, which were locally eroded by a network of distributary channels. In a transitional phase, the infilling of distributary channels and the offshore export of fine-grained sediments is related to a change in sediment sources, possibly triggered by enhanced hydrodynamic processes. The final phase involved the reworking of fluvio-deltaic sediments by shoreface processes to</p>

generate a sediment sheet. Age correlation with a suite of postglacial sea-level curves indicates that the formation of the postglacial transgressive deposits is bracketed between 14 ka and 9 ka. The studied deposits were related to a period of reduced sea-level rise, culminating in the Younger Dryas event (two oldest PTUs), and to phases of enhanced sea-level rise, such as Meltwater Pulse (MWP) 1B (two youngest PTUs). In spite of high rates of sea-level rise over MWP-1B, each PTU exhibits progradation and preservation of much of the delta. The preservation of progradational deltaic units is likely caused by increased sediment supply during progradational pulses. We suggest that those pulses of enhanced sediment fluxes during MWP-1B were strongly driven by the overall climatic conditions in the southwest of the Iberian Peninsula, probably resulting from enhanced rainfall runoff during humid periods and scarce land vegetation cover.

LRH: A. CARRIÓN-TORRENTE ET AL.

RRH: POSTGLACIAL DELTAIC PULSES IN THE GULF OF CADIZ

Research Article

DOI: 10.2110/jsr.2021.110

Episodic postglacial deltaic pulses in the Gulf of Cadiz: implications for the development of a transgressive shelf and driving environmental conditions

ÁLVARO CARRIÓN-TORRENTE,^{1,2} FRANCISCO JOSÉ LOBO,¹ ÁNGEL PUGA-BERNABÉU,² ISABEL MENDES,³ SUSANA LEBREIRO,⁴ MARGA GARCÍA,⁵ DAVID VAN ROOIJ,⁶ MARÍA LUJÁN,⁷ MARÍA ISABEL REGUERA,⁴ AND LAURA ANTÓN⁴

¹Department of Marine Geosciences, Instituto Andaluz de Ciencias de la Tierra, Spanish Research Council and University of Granada, Avenida de las Palmeras 4, 18100 Armilla, Granada, Spain

²Departamento de Estratigrafía y Paleontología, University of Granada, Granada, Spain

³Centre for Marine and Environmental Research, Universidade do Algarve, Faro, Portugal

⁴Instituto Geológico y Minero de España-Centro Nacional, Spanish Research Council, 28003, Madrid, Spain

⁵Oceanographic Centre of Cadiz, Spanish Institute of Oceanography, CSIC, Ministry of Science and Innovation, Cadiz, Spain

⁶Renard Centre of Marine Geology, Ghent University, Krijgslaan 281 (S8), 9000 Gent, Belgium

⁷Department of Earth Sciences, University of Cadiz, Puerto Real, Spain

ABSTRACT : The postglacial sea-level rise after the Last Glacial Maximum provided ideal conditions to study the transgressive sedimentary response to sudden shelf flooding driven by different rates of sea-level rise. In this study, a high-resolution seismic stratigraphic interpretation and sedimentological analysis were conducted on data from the northern Gulf of Cadiz continental shelf (SW Iberian Peninsula), in order to: 1) understand the succession of sedimentary processes during each shelf flooding episode and 2) explore the significance of variable rates of sea-level rise, sediment fluxes, and climatic conditions on the development of postglacial deposits.

Four backstepping seismic postglacial transgressive units (PTUs; 4 to 1 from oldest to youngest) that are linked to the retreating mouth of the Guadiana River were interpreted. Together, these seismic units display a wedge-shape geometry, are located over the inner to middle shelf, and overlie a regional unconformity formed during the Last Glacial Maximum. Each PTU can be divided into several sub-units with distinctive seismic facies that have a similar stratigraphic organization. Each PTU contains lower sub-units that are composed of low-angle tangential-oblique clinofolds. The clinofolds are locally topped by a channelized sub-unit. The distal and/or lateral parts of the clinofolds are occasionally buried by sheet-like semitransparent subunits. The uppermost sub-units are present over the proximal and central parts of each seismic unit and are also sheet-like. PTUs can also be subdivided and described sedimentologically. Fine-grained sands with intercalated silty layers dominate the lower part of each PTU (lower clinofold sub-units). The upper part of each PTU (upper sheet-like sub-units) is characterized by reworked

facies, composed of highly fragmented bioclasts within a mixture of silt and coarse to medium sand. Finally, mud deposits occur as a sediment drape over the PTUs.

The internal structure of each PTU reveals several phases of development under a general process of transgressive submergence in which both coastal and marine deposits were formed and eventually preserved. The initial phase involved the development of coarse-grained deltas in shallow water, which were locally eroded by a network of distributary channels. In a transitional phase, the infilling of distributary channels and the offshore export of fine-grained sediments is related to a change in sediment sources, possibly triggered by enhanced hydrodynamic processes. The final phase involved the reworking of fluvio-deltaic sediments by shoreface processes to generate a sediment sheet. Age correlation with a suite of postglacial sea-level curves indicates that the formation of the postglacial transgressive deposits is bracketed between 14 ka and 9 ka. The studied deposits are related to a period of reduced sea-level rise, culminating in the Younger Dryas event (two oldest PTUs), and to phases of enhanced sea-level rise, such as Meltwater Pulse (MWP) 1B (two youngest PTUs). In spite of high rates of sea-level rise over MWP-1B, each PTU exhibits progradation and preservation of much of the delta. The preservation of progradational deltaic units is likely caused by increased sediment supply during progradational pulses. We suggest that those pulses of enhanced sediment fluxes during MWP-1B were strongly driven by the overall climatic conditions in the southwest of the Iberian Peninsula, probably resulting from enhanced rainfall runoff during humid periods and scarce land vegetation cover.

INTRODUCTION

The sedimentary record of transgressive shorelines exhibits high variability due to the influence of various controlling factors, such as the amount and type of sediment supply, the hydrodynamic regime, the antecedent topography, and the rate of sea-level rise (Swift 1968; Nummedal and Swift 1987; Cattaneo and Steel 2003). These deposits have been identified at various spatial and temporal scales. Ancient transgressive successions are well studied in sand-dominated outcrops of limited lateral extent that provide good local documentation of key surfaces (e.g., Bergman and Snedden 1999; Cattaneo and Steel 2003; Kieft et al. 2011; Phillips et al. 2020). Research on transgressive deposits that developed during the last sea-level cycle is aided by the detailed knowledge of the glacio-eustatic sea-level pattern and paleoceanographic conditions. Postglacial transgressive deposits exhibit significant variability and can be dated at a higher resolution (e.g., Labaune et al. 2005, 2008; Nordfjord et al. 2009; Li et al. 2014; Klotsko et al. 2015; Pretorius et al. 2019), constraining the stratigraphic setting and correlating different accumulation rates in a basin (e.g., Gensous and Tesson 2003; Maselli et al. 2011; Engelbrecht et al. 2020; Dyer et al. 2021). In addition, high-resolution seismic data allow extensive mapping of key surfaces, dated with scattered sediment cores (Cattaneo and Steel 2003).

The balance between sediment supply and the intensity of ravinement in the shallow-water environment determines the depositional and erosional character of transgressions (Swift 1968). In addition, the relationship between the pattern of sea-level change and the gradient of the pre-existing topography dictates if transgressions may operate continuously due to the retreat of the shoreface or are instead punctuated by periods of

sediment accretion alternating with the drowning of coastal deposits (Cattaneo and Steel 2003). In the Gulf of Cadiz shelf, previous studies described a succession of backstepping deposits attributed to the post-Last Glacial Maximum (LGM) transgressive interval (Lobo et al. 2001; Gonzalez et al. 2004). Indeed, the study area in the Gulf of Cadiz shelf is an ideal location to evaluate the interplay between sediment supply and sea-level change. On one hand, the post-LGM sea-level rise provides exceptional conditions to study the sedimentary response to sudden shelf flooding due to the alternation of periods with different rates of sea-level rise. On the other hand, environmental conditions in the Gulf of Cadiz are characterized by locally high fluvial supplies combined with an oceanographic regime of moderate energy, representing a situation intermediate between low-energy delta-forming environments and high-energy ravinement-forming environments.

This study benefits from a substantial amount of additional data, including a very dense grid of high-resolution seismic data collected from different sources and sediment core samples in the continental shelf offshore of the Guadiana River. We aim to: 1) understand the variability and succession of sedimentary processes and systems during each shelf flooding episode under the light of existing models for transgressive development (i.e., in-place drowning, transgressive submergence, or erosional shoreface retreat) and 2) explain the differential development of postglacial deposits in response to different rates of sea-level rise, postglacial climatic variability, and sediment fluxes.

CONTEXT

Models of Development of Transgressive Deposit

Several models of transgressive deposit development have been proposed: 1) in-place drowning, 2) erosional shoreface retreat, and 3) transgressive submergence. In-place drowning involves the formation of coastal deposits followed by rapid flooding. The result of rapid flooding is the preservation of original deposits, and the amount of reworking is limited (Sanders and Kumar 1975; Rampino and Sanders 1980). This process is typical of low-gradient settings during intervals of accelerated relative sea-level rise (Cattaneo and Steel 2003). Erosional shoreface retreat describes widespread erosion as the shoreface moves landward, with a continuous, slow sea-level rise. In such cases, the preservation of coastal deposits is low, and the transgressive record is composed mainly of reworked deposits (Fisher 1961; Bruun 1962; Swift 1968, 1975, 1976; Kraft 1971). Transgressive submergence defines an intermediate situation with a lower phase of coastal deposition and an upper phase of marine reworking. This takes place during high rates of relative sea-level rise, and is common for low-gradient continental shelves with limited local sand sources in a high-energy, storm-dominated environment (Penland et al. 1988).

The Significance and Pattern of the Postglacial Transgression

The last glacial cycle contains an unusual record of high-frequency, high-amplitude sea-level oscillations driven by glacio-eustasy (e.g., Lambeck and Chappell 2001; Grant et al. 2012). In this cycle, the postglacial sea-level rise occurred after the LGM, dated globally from 26 to 19 ka (Clark et al. 2009). The rise in global mean sea level started at ~ 20 ka when the sea level was located ~ 120 m below the present level (Fig. 1; e.g., Fairbanks 1989; Bard et al. 1990, 1996; Lambeck et al. 2002; Siddall et al. 2003; Peltier

and Fairbanks 2006). This sea-level rise looks heterogeneous, where different stages related to major climate events have been identified (Fig. 1; e.g., Bard et al. 1990, 1996, 2010; Stanley 1995; Stanford et al. 2011; Lambeck et al. 2014; Peltier et al. 2015; Harrison et al. 2019).

An initial phase of ~ 10 – 15 m sea-level rise occurred between ~ 21 – 20 and 18 ka (Fig. 1; Harrison et al. 2019) followed by a short period of near-constant sea level from ~ 18 – 16.5 ka, which corresponds with the occurrence of Heinrich Event 1 (H1) (Fig. 1; Carlson and Clark 2012; Lambeck et al. 2014). Subsequently, the major phase of deglaciation occurred from ~ 16.5 – 8.2 ka, with an average rate of sea-level rise of 12 m/ka (Lambeck et al. 2014). In this interval, several phases driven by the occurrence of meltwater pulses (MWP) have been identified (e.g., Fairbanks 1989; Stanford et al. 2011; Lambeck et al. 2014). MWPs were global events involving the rapid introduction of meltwater into the ocean from ice-proximal environments as ice sheets decayed (Carlson and Clark 2012; Harrison et al. 2019).

The major phase of deglaciation (16.5 – 8.2 ka) was initiated by an ~ 25 m rise from ~ 16.5 – 15 ka (Fig. 1; Stanford et al. 2011), which was followed by a nearly constant period of sea-level stability ~ 500 – 600 yrs long. A period of high rate of sea-level rise (MWP-1A) started at ~ 14.5 ka, coinciding with the onset of the Bølling–Allerød (B-A) warm period (Fig. 1; Bard et al. 1990; Carlson and Clark 2012). The MWP-1A was characterized by an initial ~ 20 m sea-level rise with rates up to ~ 40 mm/y over ~ 500 – 600 yrs followed by another 20 m sea-level rise during 14 – 12.5 ka (Bard et al. 1996; Lambeck et al. 2014). MWP-1A was followed by an interval from ~ 12.5 – 11.5 ka of significantly reduced rates of sea-level rise, coeval to the Younger Dryas stadial (YD) in the Northern Hemisphere (Fig. 1; Bard et al. 2010). The last interval of this major phase of deglaciation (~ 11.5 – 8.8 ka) was driven by MWP-1B (Bard et al. 2010), marked by a rapid 500 yr long sea-level rise with a rate of ~ 16.5 mm/y (Fig. 1; Harrison et al. 2019). Other periods of accelerated sea-level rise (MWPs-1C and 1D) postdating MWP-1B and separated by periods of slow sea-level rise have been described in sea-level curves with a well-marked stepped pattern (e.g., Liu et al. 2004). However, the sea-level imprint of these more recent MWPs is not recorded in well-known global sea-level curves (Fig. 1; e.g., Lambeck et al. 2014). The early Holocene was characterized by a nearly uniform global rise with an average rate of ~ 15 m/ka; this phase was marked by a cooling event at 8.2 ka (Fig. 1; Stanford et al. 2011; Carlson and Clark 2012). Finally, a reduced rate of sea-level rise after 8.2 ka has been reported in a number of settings (e.g., Fairbanks 1989; Lambeck et al. 2014).

The Sedimentary Record of the Postglacial Transgression

The greatest abundance, distribution, and thickness of postglacial deposits (Fig. 2) occur in deposition-dominated continental shelves, such as the Gulf of Lions (Fig. 2A; Gensous and Tesson 2003) or the Adriatic Sea (Fig. 2B; Maselli et al. 2011) in the Mediterranean Sea. Deposition-dominated shelves are characterized by high rates of sediment supply provided by large rivers, such as the Rhône (Labaune et al. 2008) or the Po rivers (Trincardi et al. 1996). These conditions are combined with gentle topography, which results in reduced reworking, and favors sedimentary preservation (Belknap and Kraft 1985).

Lower transgressive development occurs in settings characterized by decreased sediment supplies and/or higher-energy oceanographic regimes. For example, stretches of the Californian shelves contain a reduced amount of transgressive depositional bodies than the Mediterranean cases, possibly because of lower sediment inputs (Fig. 2C; Klotsko et al. 2015). In the East China Sea, the postglacial transgressive architecture is strongly influenced by the tide-dominated hydrodynamic regime, leading to the development of tidal sand ridges (Fig. 2D; Li et al. 2014). In the Durban shelf, eastern South Africa, the increased role of currents and waves may cause the preferential development of barrier and backbarrier deposits due to increased sediment redistribution (Fig. 2E; Pretorius et al. 2016, 2019).

In erosion-dominated shelves such as the continental shelf, offshore New Jersey (Fig. 2F; Nordfjord et al. 2009), transgressive ravinement plays a major role in forming recognizable surfaces. Due to the continuous dominance of erosional processes, even during relative deep-water conditions, transgressive strata exhibit a low preservation potential (Goff et al. 2005; Nordfjord et al. 2009).

ENVIRONMENTAL SETTING

The study area is located on the northern Gulf of Cadiz continental margin, southwestern Iberian Peninsula (Fig. 3). This area comprises three well-defined physiographic domains: the continental shelf, the continental slope, and the abyssal plain (Hernández-Molina et al. 2006; Mestdagh et al. 2019). This study focuses on the transgressive deposits located on the continental shelf offshore of the Guadiana River mouth, between the narrow and relatively steep Portuguese shelf and the wider shelf on the Spanish side of the Gulf of Cadiz (Fig. 3A).

Physiography and Surface Sediments of the Shelf off the Guadiana River

The shelf offshore of the Guadiana River has a relatively flat morphology with an average gradient of 0.32° , in contrast to the steeper Portuguese shelf, where the average gradient is 0.5° . Shelf width increases from 20–25 km at the mouth of the Guadiana River to more than 30 km to the southeast (Lobo et al. 2001; Hernández-Molina et al. 2006). The shelf break occurs between 140 to 150 m water depth (Fig. 3B; Baldy 1977; Vanney and Mougenot 1981).

The continental shelf can be subdivided into three domains (inner, middle, and outer) according to the range of water depth and sediment cover (Fig. 3C; Nelson et al. 1999, Lobo et al. 2000, 2018; Maldonado et al. 2003; Gonzalez et al. 2004;). The inner shelf is covered by sandy deposits down to 25 m water depth. Proximal sandy facies are laterally bounded by scattered rocky outcrops and small muddy patches, distributed in a coast-parallel fashion (Fig. 3C; Rey and Medialdea 1989; Fernández-Salas et al. 1999). The middle shelf is located between 30 and 100 m water depth. This area is characterized by an extensive mud belt, crosscut from north to south by a sandy zone composed of muddy–gravelly sands and muddy sands, which correspond with a succession of nearshore to shallow-water sediment wedges comprising the deposits studied in this work (Fig. 3C; Gonzalez et al. 2004). The outer shelf is located below 100 m water depth. This domain exhibits mainly fine-grained deposits, such as sandy and silty clays, which are locally interrupted by coarser-grained patches of sand and gravelly sand (Fig. 3C; Nelson et al. 1999; Gonzalez et al. 2004).

Oceanographic Setting

The tidal regime is mesotidal (mean tidal range of 2.20 m) and semidiurnal along most of the northern part of the Gulf of Cadiz. The wave energy is moderate, with dominant waves approaching mainly from the W and SW (71% of occurrences). These have an average wave height of about 1 m and generate a longshore current towards the east (Del Río et al. 2012). Storm events are frequent in autumn and winter, generating significant wave heights of 4–7 m (Del Río et al. 2012; Plomaritis et al. 2015). Southwestern storms are more energetic and frequent than southeastern storms (Costa et al. 2001). Measurements of the depth of closure, i.e., the depth below which limited sediment transport due to wave action is expected to occur (Nicholls et al. 1998), on the Algarve coast provide disturbance depths up to 10 m during high-energy periods (Dolbeth et al. 2007). In other sectors of the Gulf of Cadiz, the influence of high-energy events extends to the 15–30 m water depth interval, as inferred by bedform occurrence (Gutiérrez-Mas et al. 2009).

The surface circulation in the northern Gulf of Cadiz is dominated by a branch of the Portuguese–Canary eastern boundary current that moves toward the Strait of Gibraltar (Atlantic Inflow Water, AIW; Fig. 3A). Landward, the shelf circulation between the Ria Formosa barrier system and the Guadalquivir River is characterized by cyclonic circulation (García-Lafuente et al. 2006). Inner-shelf waters (< 30 m water depth) are periodically affected by poleward coastal counter-currents (Garel et al. 2016). In contrast, the outer shelf is swept by the Gulf of Cadiz Current, which transports eastern North Atlantic Central Waters towards the southeast (Bellanco and Sánchez-Leal 2016).

Sediment Sources

Two main sources provide sediments to the Guadiana shelf: the Guadiana River and littoral drift (Gonzalez et al. 2004). The Guadiana River discharge is characterized by large intra-annual variability, with maximum levels during winter and extremely low levels in summer. The average annual suspended load of the Guadiana River, between 1946 and 1990, was $57.90 \times 10^4 \text{ m}^3/\text{yr}$, and the average annual bed load for the same time frame was $43.96 \times 10^4 \text{ m}^3/\text{yr}$ (Morales 1997).

Littoral drift carries sediments from the southern Portuguese coast to the eastern part of the Gulf of Cadiz. This results in a net eastward annual littoral drift between 10×10^4 and $30 \times 10^4 \text{ m}^3$ of mostly sandy sediments. Most of these sediments remain within the inner shelf, except for the coarser fraction, which is trapped in the Guadiana estuarine system (Gonzalez et al. 2001, 2004).

Postglacial Stratigraphy of the Gulf of Cadiz

The postglacial transgressive stratigraphy of the shelf was believed to be constituted by four backstepping seismic units (named in this study as Postglacial Transgressive Units, PTUs) (Lobo et al. 2001), which are exposed on the Guadiana shelf in the middle shelf area (Fig. 3C). However, in this work we have identified an additional PTU, summing to a total amount of five PTUs. PTUs occur seaward of a system of N–S paleochannels located on the inner-middle shelf up to 75 m water depth, eroding older Pleistocene units (Lobo et al. 2001, 2018; Gonzalez et al. 2004).

These PTUs overlie a regional unconformity formed during the LGM in the shelf sector between the Guadiana and Guadalquivir rivers (Lobo et al. 2001). The PTUs are

dominated by a mixture of quartz, bioclasts, and terrigenous components in varying proportions (Gonzalez et al. 2004). The oldest, PTU 5, is located on the outer shelf and exhibits a rather widespread lateral distribution. In contrast, the younger, PTUs 4 to 1, exhibit a more restricted distribution, confined to a sandy transgressive bathymetric high on the middle shelf (Lobo et al. 2001; Gonzalez et al. 2004).

The Holocene highstand systems tract (HST) offshore of the Guadiana Estuary mouth is composed of poorly developed subaqueous deltaic and prodeltaic muddy facies passing seaward into a number of muddy depocenters (Lobo et al. 2004, 2005; Hanebuth et al. 2018).

MATERIAL AND METHODS

The present study is based on a combined seismic stratigraphic and sedimentological analysis. In addition, eight radiocarbon (^{14}C) accelerated mass spectrometry (AMS) age dates provide chronostratigraphic constraints for placing the transgressive deposits in an evolutionary context.

Material

High-Resolution Seismic Profiling.—The main dataset used for the seismic interpretation is a set of high-resolution reflection seismic profiles acquired during two oceanographic surveys in 2013: COMIC onboard *RV Belgica*, and LASEA 2013 onboard *RV Ramón Margalef*. Two types of seismic data were acquired: parametric echo sounder (TOPAS), and sparker single-channel reflection seismic profiles. Additionally, the bathymetric information used in this study was compiled from the European Marine Observation and Data Network Bathymetry portal (EMODnet 2020) with a horizontal resolution of 115 m.

The grid of TOPAS sub-bottom seismic data consists of 1,450 km of across-shelf and along-shelf profiles from 20 m water depth to around the shelf break (Fig. 3B). TOPAS acquisition was achieved by a chirp (LFM) pulse form with transmitting frequencies of 1.5–5.5 kHz, a pulse length of 5 ms, and a power level of –2 dB. The sample rate was 30 kHz and the trace length was 200 ms. Post-processing included reflection strengthening, delay corrections, first-break picking, time-variable gain, spike removals, tide and swell static corrections, and top muting.

Seismic profiles acquired with a SIG sparker source were collected during the LASEA 2013 and COMIC 2013 surveys and provided higher penetration. Sparker profiles were collected for approximately 700 km in total, generally following or paralleling the track of the TOPAS profiles (Fig. 3B). The acquisition was made with a 300 J seismic source and a 75-m-long SIG single-channel streamer; the data resolution in the vertical domain is 1.5 m. The shot interval was 2 s, the sampling frequency was 10 kHz, and the trace length varied between 0.5 and 2s. Post-processing included correction of navigation offset, gains, bandpass filtering, demultiple, tidal and swell static corrections, and top muting.

The aforementioned data is complemented with seismic data from previous surveys in the study area, such as the GOLCA 93, FADO 96, and WADIANA 2000 surveys, which used a Uniboom source (GeopulseTM), with a cumulative total length of more than 1,500 km. The approximate vertical resolution of the system is 1–1.5 m. Basic post-processing

included bandpass filtering, amplitude corrections (spherical divergence), 2D spike removal (burst noise removal), swell static corrections, and top muting.

Sediment Cores.—The main dataset used for the sedimentological interpretation is composed of sediment cores collected in forty-five sites on the shelf offshore of the Guadiana River (Fig. 3C). Sediment cores were collected using vibrocorer, piston corer, and gravity corer devices, attaining maximum lengths of 5–6 m in specific locations. For the analysis of PTUs, 15 sediment cores were selected from seven sites acquired during the LASEA 2013 cruise (seven vibrocores (VC) (Table 1) and eight gravity cores (GC); Fig. 3C). Physical properties (magnetic susceptibility (SI) and wet density (gamma ray) in g/cc) were measured by continuous, nondestructive acquisition using a Geotech Multi-Sensor Core Logger (MSCL) at a sampling interval of 1 cm, at the Instituto Geológico y Minero de España (IGME) General Laboratories. Magnetic susceptibility of rocks is controlled by the type and amount of magnetic minerals, and wet density is mainly used to estimate the total porosity of the formation; these parameters are useful for determining subtle lithological changes.

In parallel with this analysis, high-resolution digital images of the cores were taken. Finally, the lithological description and grain size were obtained by macroscopic core visualization and the analysis of high-resolution digital images.

Radiocarbon Dating.—Eight AMS ^{14}C dates were obtained by using a mixture of benthic foraminiferal tests or different sizes of bivalve shells (Table 2), and carried out by the Poznan Radiocarbon Laboratory (Poland) using a 1.5 SDH-Pelletron Model “Compact Carbon AMS” ser. no. 003. Sample CNA3837, corresponding with PTU3, was duplicated at the CNA-Centro Nacional de Aceleradores (Seville, Spain), yielding similar ages. Age calibration was performed with the Calib 8.2 program (Stuiver et al. 2021), using the conventional radiocarbon ages and the Marine 20 calibration data set (Heaton et al. 2020). Local reservoir effect (ΔR) was not applied. The median of the probability distribution was used as a reliable estimation of the sample’s calendar age (Telford et al. 2004).

Interpretation Procedure

Seismic Interpretation.—Seismic horizons and discontinuities were interpreted following a standard seismic stratigraphy procedure (Mitchum 1977) using the commercially available software IHS Kingdom™. Each PTU was subdivided into several subunits with characteristic seismic facies (Figs. 4–7; Table 3). For visualization purposes, TOPAS profiles were preferentially used, as they provide the highest resolution and fine-scale details. Seismic-horizons and sediment-thickness grids were generated through the interpreted seismic horizons following a flex gridding algorithm in IHS Kingdom™ in order to analyze the spatial distribution of each seismic unit. These data were subsequently exported and mapped using ArcGIS™ software.

The interpretation focused on PTUs 4 to 1, from older to younger, disposed in a retrogradational stacking pattern characteristic of transgressive intervals (Catuneanu et al. 2009; Zecchin and Catuneanu 2013; Catuneanu 2019). We attempted an interpretation of transgressive stratigraphies and processes based on current knowledge of recent transgressive architectures and bounding surfaces (e.g., Trincardi et al. 1994; Saito 1994). Specifically, the wave ravinement surface (WRS), a diachronous erosional surface cut

during transgression by waves (WRS; Swift 1968; Demarest and Kraft 1987; Nummedal and Swift 1987), is significant for the reconstitution of transgressive architectures in shallow-water shelf settings.

The oldest outer-shelf transgressive unit (PTU 5 according to the new nomenclature established here) defined in Lobo et al. (2001) is excluded from this analysis. The rationale behind the exclusion is that this outer-shelf unit shows different patterns of distribution compared to the younger transgressive units. In addition, its age of formation predates the major phases of shelf transgressive flooding. Consequently, we suspect that genetic processes may be substantially different. Nevertheless, in order to constrain the chronostratigraphic framework of PTUs 4 to 1, we used the age data of PTU 5 (Lobo et al. 2015). PTUs 4 to 1 are buried by an onlapping sheet-like seismic unit with low-amplitude and subparallel to transparent seismic facies, which exhibits a widespread lateral distribution (Figs. 5A, 6A, 7A). This uppermost seismic unit has been attributed to the Holocene highstand (Lobo et al. 2004; Hanebuth et al. 2018).

Sedimentological Interpretation.—Four sediment cores (LA-25-VC, LA-22-VC, LA-48-VC, and LA-18-VC; Table 1) were selected in order to characterize the sedimentology of each PTU defined in this study (Fig. 3C). Sediment-core analysis included descriptions of the lithology, grain size, texture, sedimentary structures, bioturbation, and ultimately the definition of depositional systems. High-resolution core images were treated with Adobe Photoshop CS6 software, using the image treatment methodology proposed by Dorador et al. (2013).

RESULTS

Seismic Stratigraphy

The studied deposits cover an irregular high-amplitude horizon (called SU, Fig. 4) that marks the erosional truncation of underlying Pleistocene oblique reflections, which has been interpreted as the paleo-topography of the LGM subaerial surface (Lobo et al. 2018).

Postglacial Seismic Units (PTUs): Internal Architecture and Seismic Facies.—Each seismic unit contains a variable record of up to four different seismic sub-units (a to d) characterized by specific seismic facies and bounded by different seismic horizons (cl, clinof orm horizon; ch, channel horizon; sh, sheet horizon; rw, reworked horizon) (Fig. 4).

PTU 4 lies above the regional unconformity SU (Figs. 4, 5). Based on the seismic configuration, this unit can be divided into four sub-units: 4a, 4b, 4c, and 4d. Sub-unit 4a comprises the main body of PTU 4, and it is composed of gentle tangential-oblique clinof orms, mostly dipping southwest, with gradients $\sim 0.7^\circ$ in the foresets, decreasing distally to less than 0.2° in the bottomsets (Fig. 5B; Table 3). Over the top of the clinof orms, sub-unit 4b is locally observed infilling a scoured, channel-like horizon. It is characterized by facies with a transparent to chaotic configuration and some weak internal reflections (Table 3). Lateral to sub-unit 4a, sub-unit 4c exhibits a sheet-like morphology onlapping the clinof orms of 4a, with transparent seismic facies that extend laterally over a few kilometers (Fig. 5A; Table 3). Sub-unit 4d extends across the proximal and central part of PTU 4 over the rest of the sub-units (Fig. 5B). It shows transparent seismic facies with some weak internal reflections (Table 3) and a thin (a few meters thick) sheet-like external shape with local superimposed undulations (Fig. 5).

PTU 3 is located landward of PTU 4 (Figs. 4, 6). This unit can be divided into three sub-units: 3a, 3b, and 3d. Sub-unit 3a is characterized by a seismic facies composed of low-angle ($\sim 0.3^\circ$), parallel-oblique clinoforms dipping southwest, downlapping onto the proximal parts of PTU 4 (Fig 6B; Table 3). Over the top of sub-unit 3a, sub-unit 3b fills a scoured channel-like horizon, showing a transparent to chaotic configuration with some weak internal reflections (Table 3). Overlying these sub-units, sub-unit 3d is a thin sheet-like body located over the central part of PTU 3, with a transparent seismic configuration and scattered weak internal reflections (Table 3; Fig. 6).

PTU 2 is characterized mainly by a prograding wedge more than 20 m thick (Figs. 4, 6). The lower part of this unit is composed of two prograding bodies (i.e., sub-units 2a1 and 2a2). Both sub-units are characterized by low-amplitude tangential-oblique clinoforms with angles in the proximal zones of $\sim 1^\circ$, decreasing distally to $0.3\text{--}0.4^\circ$ (Figs. 4, 6; Table 3). These clinoforms dip in opposite directions (westward and eastward) (Fig. 6A). Sub-unit 2a1 is thinner and is completely covered by sub-unit 2a2. Lateral to this mound-shaped body, the sheet-like sub-unit 2c, with transparent seismic facies and some weak parallel internal reflections, onlaps the second prograding body (sub-unit 2a2; Fig 6A; Table 3). Sub-unit 2d extends over the proximal and central part of PTU 2 and is restricted to the eastern sector (Fig. 6A).

PTU 1 covers the proximal part of PTU 2 (Figs. 4, 7). The main core of PTU 1 is formed by three prograding sub-units (1a1, 1a2, and 1a3), which are covered by two other sub-units (1c and 1d), following a pattern similar to PTU 2. The three lower sub-units exhibit prograding configurations (Table 3). Sub-unit 1a1 is characterized by low-amplitude reflections (Fig. 7), and its upper boundary is very irregular. Sub-unit 1a2 shows a similar configuration but with gradients up to 3° . Sub-unit 1a3 is formed by low-amplitude progradational reflections with gradients up to $\sim 1^\circ$ (Fig. 7; Table 3). Sub-unit 1c shows a sheet-like external shape and onlaps laterally onto sub-unit 1a3. It is characterized by a highly transparent configuration that extends laterally over a few kilometers (Fig. 7A; Table 3). Sub-unit 1d overlies sub-unit 1a3 and is located mainly in the central and proximal areas. It is a thin (a few meters thick) sheet-like unit with transparent seismic facies and some weak internal reflections (Table 3).

Spatial Distribution.—The studied deposits are located over the inner and middle continental shelf between 40 m and 100 m water depths (Figs. 4, 8). In plan view, these units show a roughly ellipsoidal geometry (Fig. 8). Each individual unit shows wedge- or mound-shaped external shapes with a maximum thickness of 10–15 m in the central parts that decreases laterally. The depocenters of each unit are oriented $\sim N90E$, normal to the Guadiana River mouth. Nevertheless, each individual deposit varies slightly from this value.

PTU 4 is located over the middle shelf between 60 and 95 m water depth and covers an area of 212 km^2 (Fig. 8A, B). It shows an elongated $N85E$ distribution, extending 22 km in that direction and 7 km across the shelf (Fig. 8B). The main depocenter is displaced to the east, showing a maximum thickness of around 10 m.

PTU 3 is located over the middle shelf between 60 and 90 m water depth, westward in relation to PTU 4, and extends over 149 km^2 (Fig. 8A, C). Its distribution pattern is also elongated in a $N90E$ trend extending for about 18 km, whereas across the shelf it

extends for about 5.3 km (Fig. 8C). The main depocenter is located in the central area, with a maximum thickness of around 12 m.

PTU 2 is located over the inner-middle shelf between 50 and 75 m water depth (Fig. 8A, D). Its spatial distribution shows a coverage smaller (106 km²) than the previous units, extending for 14 km in the N70E direction, and less than 5 km across shelf (Fig. 8D). Its maximum thickness (~ 18 m) occurs in the central part, decreasing abruptly towards the lateral margins.

PTU 1 exhibits a restricted areal distribution (38 km²) over the inner shelf at 40–55 m water depth (Fig. 8A, E). In plan view, its distribution shows a N80E lobate shape with a maximum along-shelf length of around 8 km, and less than 5 km across shelf (Fig. 8E). The main depocenter is located slightly westward of the previous depocenters, with a maximum thickness of about 10 m (Figs. 7A, 8E).

Sedimentological Analysis

Types of Sediment Facies.—The results derived from the sedimentological analysis of sediment cores (Table 1) show that sedimentary facies in each unit exhibit a consistent pattern (Figs. 9–12). Three main types of facies are distinguished in the studied sediment cores.

Facies 1: Massive silty sands. This facies is composed of very well sorted fine-grained sands with abundant sand-size bioclasts and scattered shell fragments of centimetric scale intercalated with silty layers. Grains consist mainly of bivalve fragments and siliciclastic grains. This facies is generally massive, lacking sedimentary structures (Figs. 9F, G, 10F, 11F, G, 12G), although parallel lamination to cross-lamination (Fig. 9E), bioturbation (Fig. 10F), and mottling (Fig. 9D) are locally observed.

Facies 2: Sandy gravels. This facies comprises granule- to pebble-size bioclasts, mainly highly fragmented bivalve shells, which are hosted in a mixture of coarse to fine sand mixed with silty sand. This facies is poorly sorted and structureless (Figs. 9B, C, 10B–D, 11D, 12B).

Facies 3: Homogeneous muds. This facies consists of silt and clay without sedimentary structures and scarce well-preserved shells, some of them in life position (Figs. 9A, 10A, 11A).

Core Descriptions.—Sediment core LA-25-VC: This core is 480 cm long and penetrated PTU 4 (Figs. 3C, 5B; Table 1). From bottom to top, three intervals can be distinguished (Fig. 9). The lower interval (480–170 cm) is dominated by facies 1, where some lamination, bioturbation, mottling, and some dark layers are observed (Fig. 9D–G). Facies 1 can be assigned to sub-unit 4a. The middle interval (170–100 cm) is characterized by facies 2, whose matrix shows a darkish color compared with the rest of the core (Fig. 9B, C). This interval is also characterized by an upward, decreasing trend in the density log, continuous to the top of the core. Finally, the upper interval (100–0 cm) is characterized by homogeneous and structureless muds of facies 3. An increase in the magnetic susceptibility and a constant decrease in density is observed towards the core top. Facies 2 and 3 are correlated with post-transgressive sedimentation.

Sediment core LA-22-VC: This 440-cm-long sediment core penetrated PTU 3 (Figs. 3C, 6B; Table 1). From bottom to top, three intervals can be distinguished based on their dominant facies (Fig. 10). The lower interval (440–155 cm) is dominated by facies 1. In

the middle part of this interval, between 370 and 335 cm depth, the sand is light brownish and bioturbated (Fig. 10F). In the upper part of this interval (230–185 cm), a coarsening-upward trend in the sand matrix is accompanied by an increase in content of shell fragments (Fig. 10D). The middle interval (155–75 cm) is characterized by facies 2 (Fig. 10B, C). The lower two thirds of the core (430–130 cm), characterized by facies 1 and facies 2 toward the top, are assigned to sub-unit 3a. The uppermost interval (75–0 cm) is a package of silts and clays (Facies 3) with scattered centimetric shells (≥ 2 cm) (Fig. 10A) and where magnetic susceptibility increases steadily towards the core top. The upper 130 cm is dominated by facies 2 and 3 and corresponds to post-transgressive sedimentation.

Sediment core LA-48-VC: This sediment core corresponds with PTU 2 and is located west of the other selected cores (Figs. 3C, 6A; Table 1). It has a total length of ~ 495 cm, and two main intervals can be distinguished according to their facies (Fig. 11). The first interval (495–90 cm) shows a relatively homogeneous composition reflected in the density log (Fig. 11). This interval is characterized by facies 1, does not exhibit primary sedimentary structures, and is correlated with seismic sub-units 2c and 2a2. A grain-size increase of the sand matrix is observed in the upper part of this interval (190–90 cm) (Fig. 11B). The second interval extends along the upper part of the core (90–0 cm) and is dominated by facies 3, where well-preserved shells with sizes larger than 5 cm are found (Fig. 11A). This interval is correlated with post-transgressive sedimentation. The uppermost centimeters are characterized by a positive upward trend in magnetic susceptibility.

Sediment core LA-18-VC: This core corresponds with the uppermost part of PTU 1 (Figs. 3C, 7B; Table 1). It has a total length of about 440 cm and has a higher proportion of sand than the other sediment cores. Three intervals are distinguished according to the sedimentary facies. The lower interval (440–110 cm) is mainly dominated by facies 1, with two thin intervals characterized by facies 2 resting above erosional surfaces at 250–240 and 220–210 cm depths (Fig. 12). The second interval (110–30 cm) is characterized by facies 2 and is separated from the lower interval by a sharp erosional surface (Fig. 12B, C). This interval can be subdivided into two minor intervals. From bottom to top, the first 35 cm (110–75 cm) are characterized by a silt layer without bioclasts. This silty layer is overlain by 40 cm of highly fragmented granule to pebble-size bioclasts in a coarse to medium sand matrix, which ends abruptly in a thin (5 cm) clay layer marked by a significant increase in the magnetic susceptibility (75–30 cm) (Fig. 12). Sub-unit 1a3 is mostly dominated by facies 1 with some intervals dominated by facies 2. The uppermost interval (30–0 cm) is characterized by facies 1. Recent sedimentation shows a marked increase of the sand fraction in contrast with the other studied cores.

Age Dates

Age values (Table 2) place the formation of the postglacial transgressive deposits between 13.8 and 9 ka. However, some age dates show anomalous values older than expected taking into account the sequence of ages and the overall chronostratigraphic scenario framed by postglacial sea-level changes and associated climatic changes. We interpret these anomalous age values as the result of shell reworking, a process that is

common to other postglacial transgressive settings (e.g., Aksu et al. 2016; Pretorius et al. 2019).

INTERPRETATION AND DISCUSSION

Development of the Transgressive Stratigraphic Architecture

Depositional Environments and Processes.—In the study area, the internal organization and seismic facies of each PTU likely represent a succession of distinct depositional systems during each phase of shelf inundation bounded by flooding surfaces (Fig. 13).

The bulk of each unit is constituted by wedge-shaped, seaward-prograding clinoforms (i.e., sub-units a). Similar seismic facies have been documented in diverse postglacial transgressive architectures, where they are generically related to prograding bodies (Shinn et al. 2007; Maselli et al. 2011; Engelbrecht et al. 2020) or more specifically to ancient deltaic systems (Gensous and Tesson 2003; Labaune et al. 2005; Berné et al. 2007). Accordingly, in the study area, such clinoforms are interpreted to represent the establishment of a coastal regime, during which shallow-water, coarse-grained river-dominated deltas formed (Phase 1 in Fig. 13). This interpretation is also favored by: a) the clinoform sedimentary facies, which are predominantly constituted by silty sands, b) the fact that these transgressive clinoforms were developed seaward of an infilled incised valley attributed to the older course of the Guadiana River (Lobo et al. 2018), and c) the ages indicate that the clinoform deposits occurred in a range of water depths up to 15–20 m below contemporaneous sea levels, suggesting that clinoform development may have occurred in shallow-water environments with upward development limited by storm wave base.

Slight differences between the types of clinoforms may be related to the sandier or muddier composition of the deltaic clinoform wedges (i.e., sub-units a). Thus, the older clinoforms of PTUs 4 and 3 exhibit shallower slope and lesser amounts of sand; these facies resemble tangential-oblique or parallel-oblique deltaic progradation characteristic of muddy or moderate sand content clinothems (e.g., Gökaşan et al. 2005; Pellegrini et al. 2015; Dyer et al. 2021). In contrast, steeper and sandier clinoforms characteristic of PTUs 2 and 1 seem to be equivalent to constructional phases of sandy deltas, such as those recognized in southeast Africa offshore of the Thukela River (Engelbrecht et al. 2020).

The internal architecture of the deltaic wedges is more complex in some of the seismic units, such as PTUs 2 and 1. These units have lateral bidirectional progradation and internal truncation surfaces, interpreted to be the result of delta lobe switching and abandonment, as is found in southeast Africa transgressive deltaic bodies (e.g., Engelbrecht et al. 2020; Dyer et al. 2021).

The occasional occurrence of infilled erosional channels (i.e., sub-units b) over the proximal parts of the clinoforms is not common in postglacial transgressive architectures. Instead, similar facies are typically attributed to the topsets of lowstand deltaic deposits (Trincardi et al. 1994; Storms et al. 2008). Channel fills in the central parts of depositional bodies formed during transgressive stages have been observed in relation to radial seaward progradation and the development of fan-shaped geometries (Gökaşan et al. 2005; Engelbrecht et al. 2020). These channel units have been interpreted as delta-top distributary channels formed during phases of transgressive delta construction (Dyer et al.

2021). We favor a similar interpretation in the study area (Phase 2 in Fig. 13). The stratigraphic position and proximal location of sub-units b, in relation to the underlying clinofolds, drive us to interpret them as distributary channels formed during important normal regressions in an otherwise overall transgressive system.

Semitransparent, sheet-like facies that drape the clinofolds (i.e., sub-units c), extend beyond the edges of the underlying clinofolds. According to our knowledge, this kind of deposit and its stratigraphic relationship with underlying clinofolds is not common in other studies of transgressive deposits. Sub-units c do not completely cover the clinofolds; rather, they onlap laterally, without interfingering, and clearly postdate the clinofolds which would have been fed by the distributary channels. Consequently, a fluvial origin is not likely, and some change in the sediment sources needs to be invoked, so that these deposits can be formed above an inactive delta front. In addition, superimposed bedforms indicative of a mobile carpet (as evidenced in the Gulf of Lions, Bassetti et al. 2006) are not observed; therefore, sub-units c are also not considered to be the product of sediment reworking.

Taking into account the draping geometry and lack of internal reflections, these facies may indicate a low-energy environment dominated by mud, as documented in the South African shelf (Engelbrecht et al. 2020) or the southeastern Yellow Sea (Shinn et al. 2007). Since these sub-units c are found down-dip of the channelized facies (sub-units b), a process of sediment partitioning could have taken place, involving retention of the coarse-grained fraction in the distributary channels, and coeval offshore fine-grained sediment dispersal by the action of oceanographic agents such as waves, tides, and/or currents (Phase 3 in Fig. 13). We propose that sub-units c could be interpreted as the result of a type of sediment gravity flow induced either by wave (wave-supported gravity flows) or tidal motions (estuarine fluid muds) (e.g., Parsons et al. 2007). The winnowing of fine-grained sediments in the distributary channels would form sediment plumes in the shelf environment, which would be eventually redistributed laterally by the Gulf of Cadiz Current (Bellanco and Sánchez-Leal 2016), leading to the generation of extensive mud blankets far beyond the confined location of the deltaic clinofolds.

Upper chaotic facies documented in a number of paleo-deltaic systems are interpreted as sandy bedforms originated from ancient shorelines or delta fronts (e.g., Berné et al. 2007). However, in the study area the uppermost sub-units d in each seismic unit occur over erosional truncations. Truncations on top of underlying clinofolds are interpreted as the product of ravinement (Shinn et al. 2007). The sub-units observed over the truncations closely resemble the pattern identified on several sectors of the Italian shelves, where sheet-like transparent units are interpreted as reworked (lower shoreface) sand sheets (Tortora 1996). These sheets may develop asymmetric patterns on their tops, interpreted as dunes formed during the reworking of the sandy layer (Masselli et al. 2011). Similarly, in our study area, these upper sub-units are considered as the by-product of the reworking of the original clinofolds during transgressive ravinement (Phase 4 in Fig. 13), generating scattered bedforms along the central area of sub-unit 4d (Fig. 5).

The observed architectures in the studied PTUs are in agreement with the preservation of both paralic (coastal) and marine components that compose transgressive deposits (Saito 1994; Tortora 1996). However, PTUs identified on the Guadiana shelf

exhibit a diverse and rich internal stratigraphic organization, unparalleled in many other postglacial transgressive deltaic systems that tend to exhibit, as a general rule, a more monotonous stratigraphy and composition (e.g., Gensous and Tesson 2003; Maselli et al. 2011)

In the present study, the lower component would be composed of shallow-water deltaic clinofolds and facies associated with the full establishment of fluvio-deltaic depositional systems (seismic facies or sub-units a). The upper chaotic facies with local development of undulations would represent marine deposits as a consequence of transgressive ravinement (seismic sub-units d).

However, in the study area the transition between the deltaic systems and the marine deposits would be more complex than in other transgressive settings. Such transition is represented not only by a wave ravinement surface but also by a significant change of sediment sources involving the dearth of deltaic construction and the establishment of a process of sediment partitioning involving channel infilling and offshore export of fine-grained sediments (seismic sub-units b and c).

Implications for Transgressive Development.—The postglacial sedimentary record on the Guadiana shelf displays several distinct characteristics in terms of the preservation and internal architecture of individual deposits in transgressive deltaic settings. A number of indications would signal the importance of high sediment fluxes during each transgressive phase. These indications include: a) an unusually large number of transgressive deposits, b) occurrence of proximal infilled channels, and c) occurrence of delta lobe switching.

Many transgressive shelf-wide settings are low-accumulation settings due to the strong prevalence of transgressive ravinement. As a consequence, Atlantic transgressive settings tend to be composed of erosional morphologies, such as coastal terraces, transgressive lags and bedforms, and/or remnants of coastal deposits such as barriers (e.g., Nordfjord et al. 2009; Cooper et al. 2016; Ximenes Neto et al. 2018; Gomes et al. 2020). Preservation of single transgressive wedges has been reported on the New Jersey shelf (Nordfjord et al. 2009) and the Galician shelf (Lantsch et al. 2010). The dominance of transgressive ravinement may even occur on wide shelves, where the development of deltaic deposits in the transgressive systems tract is also uncommon (Puchala et al. 2011).

Transgressive packages also exhibit low preservation potential of deltaic deposits on shelves fed by short, mountainous streams such as the Californian shelf (Spinelli and Field 2003; Hogarth et al. 2012). There, clinofold wedges of restricted distribution have been identified in specific sectors (Grossman et al. 2006; Klotsko et al. 2015). Also, the well-studied transgressive record of the South African shelf is strongly dominated by nondeltaic shoreline-connected deposits (e.g., Pretorius et al. 2019; Green et al. 2020). However, in river-dominated sectors of the southeastern African shelf, several phases of transgressive deltaic progradation have been reported to occur intercalated within the major postglacial shelf flooding phases (Engelbrecht et al. 2020; Dyer et al. 2021).

Significant development of transgressive deltaic deposits in water depths equivalent to those of the study area, and with transgressive ages younger than 14.5 ka, is found only in several Mediterranean settings. These settings are regarded as ideal delta-forming environments, due to the sediment supply conditions and redistribution of river-borne

sediments by oceanographic processes (Anthony et al. 2014). For example, three individual deposits have been described in the Gulf of Lions (Gensous and Tesson 2003; Labaune et al. 2005) and two to three individual transgressive deposits in the Adriatic Sea (Storms et al. 2008; Maselli et al. 2011).

In comparison to all those settings, the number (four) of transgressive deposits identified in the middle to inner shelf setting of the study area seems to be higher, and would imply faster responses of the Guadiana fluvial system to external driving factors in comparison to the sedimentary response of larger fluvial systems, such as the Po or the Rhône river systems. Other stratigraphic evidence that suggests a significant influence of fluvio-deltaic processes include the presence of proximal distributary channels on top of the clinofolds and identification of delta switching processes in the younger PTUs. The identification of delta-top distributary channels in postglacial transgressive architectures has been related with extensive periods of delta progradation under normal regressive conditions (Dyer et al. 2021). We favor that interpretation in the study area, because these distributary channels are identified in PTUs 4 and 3, whose formation is related to a prolonged sea-level slowdown (see subsequent discussion about sea-level change trends). Delta lobe switching and abandonment occurring in an overall transgressive context can be produced by pure autocyclic processes, due to lateral shifting of river courses (Berné et al. 2007; Zecchin et al. 2015; Dyer et al. 2021). However, such a hypothesis cannot be tested in the study area, because evidence of delta lobe switching are restricted to the younger PTUs 2 and 1, where preserved distributary channels are not found.

Alternatively, delta lobe switching has also been related to changing sediment fluxes to the deltaic realm due to variations in the frequency and magnitude of flood events driven by transitions between humid and dry climates (Berné et al. 2007; Dyer et al. 2021). A similar interpretation could be valid for PTUs 2 and 1, since their formation is roughly coeval with a period of increased frequency of large-magnitude floods after the Younger Dryas event in southern Iberia (more details in a subsequent discussion about the role of sediment fluxes).

Another significant difference between the postglacial record of the Guadiana shelf and most Mediterranean settings, which exhibit similar arrangements of transgressive stacking patterns, is the formation of reworked facies overlying prodeltaic clinofolds. In most Mediterranean examples, these facies are poorly documented at the seismic scale (e.g., Gensous and Tesson 2003; Berné et al. 2007; Maselli et al. 2011). This significant difference could be explained by considering the oceanographic setting. Several facts would account for the distinctive influence of the oceanographic regime in the Gulf of Cadiz:

- In the present-day Gulf of Cadiz, wave remobilization may extend to several tens of meters water depths (e.g., Dolbeth et al. 2007; Gutiérrez-Mas et al. 2009).
- The estimated water depth of the Gulf of Cadiz transgressive clinofolds, in relation to coeval sea levels, indicate wave-base levels 10–20 m deep.
- The Guadiana shelf clinofolds exhibit a heterolithic coarse-grained composition, in contrast to other Mediterranean clinofolds, which tend to be finer-grained (Pellegrini et al. 2015).

- The elongated depocenters of each unit, specially marked in PTUs 4 and 3, would attest to the influence of an active shelf current circulation, represented at present day by the dominant Gulf of Cadiz Current (Bellanco and Sánchez-Leal 2016).

Therefore, the sedimentary architecture of the postglacial transgressive deposits in the Guadiana shelf area resulted from the combination of relatively significant fluvial sediment fluxes and a wave-dominated setting with active along-shelf currents, in contrast to most Mediterranean settings where: a) possibly, the larger drainage basins were less dynamic in their sedimentary response, and b) hydrodynamic conditions were of lower energy. As a consequence, the observed architecture of the postglacial transgressive deposits is more compatible with a transgressive submergence process rather than with a process of in-place drowning (i.e., overstepping), which seems to be the preferential mechanism in transgressive records dominated by the preservation of barriers and associated deposits (e.g., Pretorius et al. 2019; Green et al. 2020).

Chronological Framework of the Postglacial Transgression: Implications for Driving Processes

The Importance of Sea-Level Change Trends.—The occurrence of each phase of transgressive development and the sea-level pattern in continental shelves shows a great diversity around the world. In general terms, under the absence or scarcity of age control, depths of occurrence of transgressive deposits or shorelines are compared with the glacio-eustatic stepped sea-level rise (Fig. 14). With such constraints, major phases of clinoform development are assumed to be related with periods of reduced sea-level rise or stillstands (Zecchin et al. 2015) such as the Younger Dryas (Gensous and Tesson 2003; Boyer et al. 2005; Berné et al. 2007; Maselli et al. 2011), or during steps punctuating MWP (Zecchin et al. 2015; Engelbrecht et al. 2020; De Santis et al. 2020; Dyer et al. 2021). In wave-dominated settings, shoreline complexes have also been related to sea-level stability (Green et al. 2014). Under that scheme, major periods of shelf drowning are supposed to be driven by periods of enhanced sea-level rise, such as MWPs-1A and 1B (Fig. 14) (Pellegrini et al. 2015; Green et al. 2014; Zecchin et al. 2015).

However, the development of transgressive deposits also occurs during moderately high rates of sea-level rise (up to 10 mm/year). This occurs during the sea-level rise postdating the Younger Dryas (Berné et al. 2007) and during the sea-level deceleration after MWP-1B (Fig. 14) (Gensous and Tesson 2003; Boyer et al. 2005; Storms et al. 2008; Schattner et al. 2020; Maselli et al. 2011; De Falco et al. 2015).

In the most extreme cases, the development of transgressive deposits has even been related to periods of sustained sea-level rises with rates up to 60 mm/year during the MWP-1A (Fig. 14). For example, coastal barrier-lagoon systems (Storms et al. 2008; De Santis et al. 2020) and prograding bodies (Maselli et al. 2011) have been reported in the Adriatic Sea, and low-energy marine deposits in the Gulf of Lions (Labaune et al. 2005). In California, the generation of a clinoform wedge was also related to the abrupt sea-level rise of MWP-1B (Fig. 14) (Grossman et al. 2006).

The formation of the studied PTUs 4 to 1 is framed by the overall sea-level rise in the 14–9 ka interval (Fig. 14). In general, most of the ages exhibit a coherent pattern; however, some anomalous results provide ages older than expected, with values located

well above the contemporary sea-level positions (Fig. 14, Table 2). One of the anomalous results corresponds with the age value of PTU 4 (16.3 ka, Fig. 14, Table 2), which is considerably older than the termination age of preceding PTU 5, framed between 13.8 and 14.3 ka (Lobo et al. 2015). The ages of the younger PTU 3 between 11.2 and 12.7 ka are in agreement with a genesis during the Younger Dryas event, a period of reduced sea-level rise (Fig. 14, Table 2). Consequently, we infer that the formation of PTU 4 occurred between 12.7 and 13.8 ka, possibly during MWP-1A but after the phase of accelerated sea-level rise between 14.5 and 14 ka (Stanford et al. 2011; Lambeck et al. 2014). Conversely, the ages of the most recent PTUs (2 and 1) would place them in a period of high rates of sea-level rise during MWP-1B, between 11.5 and 8.8 ka (Stanford et al. 2011).

The proposed chronological framework supports the idea that PTUs 4 and 3 are genetically related, and that PTUs 2 and 1 are also genetically related. Thus, the formation of PTUs 4 and 3 possibly took place in an interval bracketed by two periods of very high sea-level rise during MWPs-1A and 1B, when rates of sea-level rise were generally lower than 15 mm/year (Stanford et al. 2011). Therefore, these two units are related to a period of deceleration or slowdown during the deglaciation that culminated in the Younger Dryas event. This is similar to other transgressive settings such as the Gulf of Lions or the Adriatic Sea (Gensous and Tesson 2003; Maselli et al. 2011). These periods of reduced sea-level rise are assumed to be related to major phases of clinof orm development (Zecchin et al. 2015). This is compatible with our observations, since these two older transgressive units exhibit more elongated patterns, wider distribution and a finer-grained composition than the two younger units, suggesting genetic conditions favorable for clinof orm development.

In contrast to the sea-level conditions of the older transgressive deposits, the two more recent PTUs (2 and 1) are assumed to be related to an overall period of enhanced sustained sea-level rise during MWP-1B, with rates of sea-level change of around 20 mm/year and even higher (Stanford et al. 2011). This connection with high rates of sea-level rise is also reflected in the geometry and composition of such units, which are more confined and exhibit higher percentages of sands than the older transgressive deposits.

The Role of Sediment Fluxes in the River Basin.—As discussed above, the formation of PTUs 2 and 1 seems to be related with high rise rates of sea level. Indeed, under such circumstances, major increases in sediment supply may guide the formation of postglacial transgressive deposits rather than the primary control of sea-level changes. These changes in sediment flux might have been the result of rapid climatic changes (Berné et al. 2007; Labaune et al. 2008) influencing vegetation cover and subsequently the total discharge (Maselli et al. 2011). Other interpretations stress the importance of: a) antecedent slope and geology, as they may influence the rate of transgression and the ravinement processes, particularly in transgressive systems composed mainly of barriers (Storms et al. 2008; Pretorius et al. 2016) and b) uplift rates greater than sea-level rise rates (Grossman et al. 2006; Hogarth et al. 2012).

Assuming preferential development during conditions of rapid sea-level rise, phases of increased precipitation and sediment input have been invoked to trigger the development of deltaic deposition during transgressive intervals (Puchala et al. 2011).

Specifically, phases of enhanced sediment supply could have been fostered by meltwater pulses (Labaune et al. 2008; Lebreiro et al. 2009). With relevance for the study area, periods of increased fluvial activity in Spain related to anomalous rainfall (Trigo and DaCamara 2000) extend back to the postglacial transgression. In fact, the two older periods of increased frequency of large-magnitude floods postdate the Younger Dryas event (10.75–10.24 and 9.62–8.785 ka) (Thorndycraft and Benito 2006; Benito et al. 2008). The increase in flood frequency after the Younger Dryas event has been related to large-scale atmospheric circulation changes and climatic transitions (Benito et al. 2008) in relation to the return of westerly storm tracks to Iberian latitudes (Thorndycraft and Benito 2006). After these two main flooding periods, a hiatus in the paleoflood record until 2.9 ka, with no major increases in the flood frequency, has been reported (Thorndycraft and Benito 2006).

These flooding phases probably involved spatially diverse climatic trends, with colder and more arid climates in central Iberia and more temperate and humid in western (Morellón et al. 2018), southwestern (Dorado Valiño et al. 2002), and southern (Mesa-Fernández et al. 2018) Iberia. In fact, the period between 10.8 and 7 ka is regarded as dominated by increasingly humid conditions in western and southern Iberia, with enhanced runoff inputs interrupted by arid events (Carrión 2002; Rodrigues et al. 2009 2010; Mesa-Fernández et al. 2018; Morellón et al. 2018).

At a smaller scale and with relevance for the present study, expansions and declines of forests in the Guadiana Estuary since 13 ka provide indications of climatic variability. Temperate to warm, moist climates occurred during the Allerød interstadial and between 9 and 5 ka. Drier conditions were prevalent during the Younger Dryas and the early Holocene (Fletcher et al. 2007). These general climatic conditions in SW Iberia seem to be in agreement with our chronostratigraphic scenario, assuming that sediment supply in the southern Iberian Peninsula is strongly driven by rainfall during humid periods because the land vegetation cover is scarce. Thus, we relate the formation of PTUs 2 and 1 postdating the Younger Dryas event to humid climates prevailing in SW Iberia, and by extension, in the Guadiana drainage basin. Conditions of increased humidity during the early Holocene after the Younger Dryas event possibly accentuated allocyclic processes, leading to channel abandonment and delta lobe switching during the younger PTUs. Also in the Guadiana Estuary, an accelerated phase of infilling by clayey sediments was initiated at ca. 9.8 ka (Boski et al. 2002). This trend also seems to be compatible with the transgressive record on the shelf, since the formation of PTUs 2 and 1, which exhibit a sandier composition than the older transgressive deltas, occurred at the timing of fine-grained sediment trapping in the estuary.

CONCLUSIONS

The rich stratigraphic architecture of four postglacial transgressive units (PTUs) recognized in the northern margin of the Gulf of Cadiz off the Guadiana River reveals the occurrence of several major phases of development, indicating a high variability in the driving factors in the Gulf of Cadiz; in contrast, many other postglacial transgressive settings tend to be largely dominated by a prevailing controlling factor, such as fluvial sediment supply, hydrodynamic activity, or antecedent topography, resulting in generally more homogeneous sedimentary processes and products.

The initial phase was the establishment of shallow-water, coarse-grained, river-dominated deltas. These deltas were subsequently eroded by distributary channels formed during normal regressions, punctuating the overall transgressive interval. Transitional phases between normal regressions and resumed transgressions involved the filling of distributary channels and the offshore export and lateral redistribution of fine-grained sediments due to enhanced hydrodynamic activity. The last phase was driven by shoreface reworking of previous fluvio-deltaic depositional systems and the formation of wave-ravinement surfaces. The sedimentary architecture of the postglacial transgressive deposits on the Guadiana shelf involves both enhanced deposition as well as subsequent preservation of reworked facies. This stratigraphic pattern likely resulted from the combination of relatively significant sediment fluxes generating normal regressions during different rates of sea-level rise and an active oceanographic regime with wave and/or tidal reworking in the nearshore and along-shelf redistribution by currents. As a result, the observed transgressive architectures are best explained by a transgressive submergence process.

The formation of PTUs located on the Guadiana Shelf is framed within the 14–9 ka interval; the chronostratigraphic framework provides important clues to the variable influences of controlling factors of transgressive development, suggesting that both rates of sea-level rise and sediment fluxes played significant yet contrasting roles. Thus, the older PTUs (4 and 3) seem to be related to periods of reduced sea-level rise, such as the terminal part of MWP-1A and the Younger Dryas event. Meanwhile, the younger PTUs (2 and 1) are related with the MWP-1B, a period of high rate of sea-level rise during the deglaciation.

The genesis of PTUs 2 and 1 is attributed primarily to the overall climatic conditions established in SW Iberia after the Younger Dryas that triggered significant changes in sediment supply in the river basin. Those phases of enhanced sediment supply probably resulted from increased rainfall runoff during humid periods and scarce land vegetation cover.

The prevailing influence of those controlling factors has been modified through time, and is reflected in the morphology, distribution patterns, and lithologies of PTUs. Thus, more extended deposit distributions and fine-grained compositions tend to occur during enhanced sea-level dominance. In contrast, more confined distributions and coarse-grained compositions seem to be the result of enhanced sediment fluxes.

ACKNOWLEDGMENTS

This study received financial support by the Spanish Ministry of Economy and Competitiveness, projects CGL2011-30302-C02-02 and CTM2017-88237-P. We thank the hard work done by the crew, scientists, and technicians on board Spanish *RV Ramón Margalef* during the LASEA survey and Belgian *RV Belgica* during the COMIC survey. Shiptime on *RV Belgica* was provided by BELSPO and RBINS–OD Nature. Seismic interpretations were made using IHS Kingdom™ software, thanks to the participation of the Instituto Andaluz de Ciencias de la Tierra in the IHS University Grant program. I. Mendes thanks to Fundação para a Ciência e a Tecnologia for Research Assistant contract DL57/2016/CP1361/CT0009 and project UID/0350/2020 CIMA. Thanks are also extended to external reviewers Andy Green and Stephen Phillips for their detailed

and constructive comments which improved a previous version of the manuscript, as well as to journal editors Kathleen M. Marsaglia and Tobi Payenberg for their general remarks.

REFERENCES

Aksu, A.E., Hiscott, R.N., and Yaltrak, C., 2016, Early Holocene age and provenance of a mid-shelf delta lobe south of the Strait of Bosphorus, Turkey, and its link to vigorous Black Sea outflow: *Marine Geology*, v. 380, p. 113–137.

Anthony, E.J., Marriner, N., and Morhange, C., 2014, Human influence and the changing geomorphology of mediterranean deltas and coasts over the last 6000 years: from progradation to destruction phase?: *Earth Science Reviews*, v. 139, p. 336–361.

Baldy, P., 1977, *Géologie du plateau continental portugaise (au sud du cap de Sines)* [Thèse de 3ème Cycle] : Université Paris VI, 113 p.

Bard, E., Hamelin, B., and Fairbanks, R.G., 1990, U-Th ages obtained by mass-spectrometry in corals from Barbados: sea-level during the past 130,000 years: *Nature*, v. 346, p. 456–458.

Bard, E., Hamelin, B., Arnold, M., Montaggioni, L., Cabioch, G., Faure, G., and Rougerie, F., 1996, Deglacial sea-level record from Tahiti corals and the timing of global meltwater discharge: *Nature*, v. 382, p. 241–244.

Bard E., Hamelin B., and Delanghe-Sabatier D., 2010, Deglacial meltwater pulse 1B and Younger Dryas sea levels revisited with boreholes at Tahiti: *Science*, v. 327, p. 1235–1237.

Bassetti, M.A., Jouet, G., Dufois, F., Berné, S., Rabineau, M., and Taviani, M., 2006, Sand bodies at the shelf edge in the Gulf of Lions (Western Mediterranean): Deglacial history and modern processes: *Marine Geology*, v. 234, p. 93–109.

Belknap, D.F., and Kraft, J.C., 1985, Influence of antecedent geology on stratigraphic preservation potential and evolution of Delaware's barrier systems: *Marine Geology*, v. 63, p. 235–262.

Bellanco, M.J., and Sánchez-Leal, R.F., 2016, Spatial distribution and intra-annual variability of water masses on the Eastern Gulf of Cadiz seabed: *Continental Shelf Research*, v. 128, p. 26–35.

Benito, G., Thorndycraft, V.R., Rico, M., Sánchez-Moya, Y., and Sopena, A., 2008, Palaeoflood and floodplain records from Spain: evidence for long-term climate variability and environmental changes: *Geomorphology*, v. 101, p. 68–77.

Bergman, K.M., and Snedden, J.W., 1999, *Isolated Shallow Marine Sand Bodies: Sequence Stratigraphic Analysis and Sedimentologic Interpretation*: SEPM, Special Publication, 64, 362 p.

Berné, S., Jouet, G., Bassetti, M.A., Dennielou, B., and Taviani, M., 2007, Late Glacial to Preboreal sea-level rise recorded by the Rhône deltaic system (NW Mediterranean): *Marine Geology*, v. 245, p. 65–88.

Boski, T., Moura, D., Veiga-Pires, C., Camacho, S., Duarte, D., Scott, D.B., and Fernandes, S.G., 2002, Postglacial sea-level rise and sedimentary response in the Guadiana Estuary, Portugal/Spain border: *Sedimentary Geology*, v. 150, p. 103–122.

- Boyer, J., Duvail, C., Le Strat, P., Gensous, B., and Tesson, M., 2005, High resolution stratigraphy and evolution of the Rhône delta plain during Postglacial time, from subsurface drilling data bank: *Marine Geology*, v. 222–223, p. 267–298.
- Bruun, P., 1962, Sea level rise as a cause of shore erosion: *American Society of Civil Engineers, Proceedings*, v. 88, p. 117–130.
- Carlson, A.E., and Clark, P.U., 2012, Ice sheet sources of sea-level rise and freshwater discharge during the last deglaciation: *Reviews of Geophysics, Journal of the Waterways and Harbour Division*, v. 50, p. 1–72.
- Carrión, J.S., 2002, Patterns and processes of Late Quaternary environmental change in a montane region of southwestern Europe: *Quaternary Science Reviews*, v. 21, p. 2047–2066.
- Cattaneo, A., and Steel, R.J., 2003, Transgressive deposits: a review of their variability: *Earth-Science Reviews*, v. 62, p. 187–228.
- Catuneanu, O., 2019, Model-independent sequence stratigraphy: *Earth-Science Reviews*, v. 188, p. 312–388.
- Catuneanu, O., Abreu, V., Bhattacharya, J.P., et al., 2009, Towards the standardization of sequence stratigraphy: *Earth-Science Reviews*, v. 92, p. 1–33.
- Clark, P.U., Dyke, A.S., Shakun, J.D., Carlson, A.E., Clark, J., Wohlfarth, B., Mitrovica, J.X., Hostetler, S.W., and McCabe, A.M., 2009, The last Glacial Maximum: *Science*, v. 325, p. 710–714.
- Cooper, J.A.G., Green, A.N., Meireles, R.P., Klein, A.H.F., Souza, J., and Toldo, E.E., 2016, Sandy barrier overstepping and preservation linked to rapid sea-level rise and geological setting: *Marine Geology*, v. 382, p. 80–91.
- Costa, M., Silva, R., and Vitorino, J., 2001, Contribuição para o estudo do clima de agitação marítima na costa Portuguesa: Sines, Portugal, 2as Jornadas Portuguesas de Engenharia Costeira e Portuária, *Proceedings, CD-ROM*.
- De Falco, G., Antonioli, F., Fontolan, G., Lo Presti, V., Simeone, S., and Tonielli, R., 2015, Early cementation and accommodation space dictate the evolution of an overstepping barrier system during the Holocene: *Marine Geology*, v. 369, p. 52–66.
- De Santis, V., Caldara, M., and Pennetta, L., 2020, Transgressive architecture of coastal barrier systems in the Ofanto incised valley and its surrounding shelf in response to stepped sea-level rise: *Geosciences*, v. 10, no. 497.
- Del Río, L., Plomaritis, T.A., Benavente, J., Valladares, M., and Ribera, P., 2012, Establishing storm thresholds for the Spanish Gulf of Cádiz coast: *Geomorphology*, v. 143–144, p. 13–23.
- Demarest, J.M., Kraft, J.C., 1987, Stratigraphic record of Quaternary sea levels: implications for more ancient strata, *in* Nummedal, D., Pilkey, O.H., and Howard, J.D., eds., *Sea-Level Fluctuation and Coastal Evolution: SEPM, Special Publication 41*, p. 223–239.
- Dolbeth, M., Ferreira, Ó., Teixeira, H., Marques, J.C., Dias, J.A., and Pardal, M.A., 2007, Beach morphodynamic impact on a macrobenthic community along a subtidal depth gradient: *Marine Ecology, Progress Series*, v. 352, p. 113–124.

- Dorador, J., and Rodríguez-Tovar, F.J., and IODP Expedition 339 Scientists, 2013, Digital image treatment applied to ichnological analysis of marine core sediments: *Facies*, v. 60, p. 39–44.
- Dorado Valiño, M., Valdeolmillos Rodríguez, A., Blanca Ruiz Zapata, M., José Gil García, M., and de Bustamante Gutiérrez, I., 2002, Climatic changes since the Late-glacial/Holocene transition in La Mancha Plain (South-central Iberian Peninsula, Spain) and their incidence on Las Tablas de Daimiel marshlands: *Quaternary International*, v. 93–94, p. 73–84.
- Dyer, S.E., Green, A.N., Cooper, J.A.G., Hahn, A., and Zabel, M., 2021, Response of a wave-dominated coastline and delta to antecedent conditioning and fluctuating rates of postglacial sea-level rise: *Marine Geology*, v. 434, no. 106435.
- EMODnet Bathymetry Consortium, 2020, EMODnet Digital Bathymetry (DTM): EMODnet Bathymetry Consortium.
- Engelbrecht, L., Green, A.N., Cooper, J.A.G., Hahn, A., Zabel, M., and Mackay, C.F., 2020, Construction and evolution of submerged deltaic bodies on the high energy SE african coastline: the interplay between relative sea level and antecedent controls: *Marine Geology*, v. 424, no. 106170.
- Fairbanks, R.G., 1989, A 17,000-year glacio-eustatic sea level record: influence of glacial melting rates on the Younger Dryas event and deep-ocean circulation: *Nature*, v. 342, p. 637–642.
- Fernández-Salas, L.M., Rey, J., Pérez-Vazquez, E., Ramírez, J.L., Hernández-Molina, F.J., Somoza, L., De Andrés, J.R., and Lobo, F.J., 1999, Morphology and characterization of the relict facies on the internal continental shelf in the Gulf of Cadiz between Ayamonte and Huelva (Spain): *Instituto Español de Oceanografía, Boletín*, v. 15, p. 123–132.
- Fisher, A.G., 1961, Stratigraphic record of transgressing seas in light of sedimentation on Atlantic coast of New Jersey: *American Association of Petroleum Geologists, Bulletin*, v. 45, p. 1656–1667.
- Fletcher, W.J., Boski, T., and Moura, D., 2007, Palynological evidence for environmental and climatic change in the lower Guadiana valley, Portugal, during the last 13,000 years: *The Holocene*, v. 17, p. 481–494.
- García-Lafuente, J., Delgado, J., Criado-Aldeanueva, F., Bruno, M., del Río, J., and Miguel Vargas, J., 2006, Water mass circulation on the continental shelf of the Gulf of Cádiz: *Deep Sea Research Part II: Topical Studies in Oceanography*, v. 53, p. 1182–1197.
- Garel, E., Laiz, I., Drago, T., and Relvas, P., 2016, Characterisation of coastal counter-currents on the inner shelf of the Gulf of Cádiz: *Journal of Marine Systems*, v. 155, p. 19–34.
- Gensous, B., and Tesson, M., 2003, L’analyse des dépôts postglaciaires et son application à l’étude des séquences de dépôt du Quaternaire terminal sur la plate-forme au large du Rhône (Golfe du Lion) : *Société Géologique de France, Bulletin*, v. 174, p. 401–419.
- Goff, J.A., Austin, J.A., Jr., Gulick, S., Nordfjord, S., Christensen, B., Sommerfield, C., Olson, H., and Alexander, C., 2005, Recent and modern marine erosion on the New Jersey outer shelf: *Marine Geology*, v. 216, p. 275–296.

- Gökaşan, E., Tur, H., Ecevitoglu, B., Görüm, T., Türker, A., Tok, B., Çağlak, F., Birkan, H., and Şimşek, M., 2005, Evidence and implications of massive erosion along the Strait of İstanbul (Bosphorus): *Geo-Marine Letters*, v. 25, p. 324–342.
- Gomes, M.P., Vital, H., and Droxler, A.W., 2020, Terraces, reefs, and valleys along the Brazil northeast outer shelf: deglacial sea-level archives?: *Geo-Marine Letters*, v. 40, p. 699–711.
- Gonzalez, R., Dias, J.M.A., and Ferreira, Ó., 2001, Recent rapid evolution of the Guadiana Estuary (Southern Portugal/Spain): *Journal of Coastal Research*, Special Issue 34, p. 516–527.
- Gonzalez, R., Dias, J.A., Lobo, F., and Mendes, I., 2004, Sedimentological and paleoenvironmental characterisation of transgressive sediments on the Guadiana Shelf (Northern Gulf of Cadiz, SW Iberia): *Quaternary International*, v. 120, p. 133–144.
- Grant, K.M., Rohling, E.J., Bar-Matthews, M., Ayalon, A., Medina-Elizalde, M., Ramsey, C.B., Satow, C., and Roberts, A.P., 2012, Rapid coupling between ice volume and polar temperature over the past 150,000 years: *Nature*, v. 491, p. 744–747.
- Green, A.N., Cooper, J.A.G., and Salzmann, L., 2014, Geomorphic and stratigraphic signals of postglacial meltwater pulses on continental shelves: *Geology*, v. 42, p. 151–154.
- Green, A.N., Cooper, J.A.G., Dlamini, N.P., Dladla, N.N., Parker, D., and Kerwath, S.E., 2020, Relict and contemporary influences on the postglacial geomorphology and evolution of a current swept shelf: The Eastern Cape Coast, South Africa: *Marine Geology*, v. 427, no. 106230.
- Grossman, E.E., Eitrem, S.L., Field, M.E., and Wong, F.L., 2006, Shallow stratigraphy and sedimentation history during high-frequency sea-level changes on the central California shelf: *Continental Shelf Research*, v. 26, p. 1217–1239.
- Gutiérrez-Mas, J.M., Juan, C., and Morales, J.A., 2009, Evidence of high-energy events in shelly layers interbedded in coastal Holocene sands in Cadiz Bay (south-west Spain): *Earth Surface Processes and Landforms*, v. 34, p. 810–823.
- Hanebuth, T.J.J., King, M.L., Mendes, I., Lebreiro, S., Lobo, F.J., Oberle, F.K., Antón, L., Ferreira, P.A., and Reguera, M.I., 2018, Hazard potential of widespread but hidden historic offshore heavy metal (Pb, Zn) contamination (Gulf of Cadiz, Spain): *Science of The Total Environment*, v. 637–638, p. 561–576.
- Harrison, S., Smith, D.E., and Glasser, N.F., 2019, Late Quaternary meltwater pulses and sea level change: *Journal of Quaternary Science*, v. 34, p. 1–15.
- Heaton, T.J., Köhler, P., Butzin, M., Bard, E., Reimer, R.W., Austin, W.E.N., Bronk Ramsey, C., Grootes, P.M., Hughen, K.A., Kromer, B., Reimer, P.J., Adkins, J., Burke, A., Cook, M.S., Olsen, J., and Skinner, L.C., 2020, Marine20: the marine radiocarbon age calibration curve (0–55,000 cal BP): *Radiocarbon*, v. 62, p. 779–820.
- Hernández-Molina, F.J., Llave, E., Stow, D.A.V., Garcia, M., Somoza, L., Vazquez, J.T., Lobo, F.J., Maestro, A., del Rio, V.D., Leon, R., Medialdea, T., and Gardner, J., 2006, The contourite depositional system of the Gulf of Cadiz: a sedimentary model related to the bottom current activity of the Mediterranean outflow water and its interaction with the continental margin: *Deep-Sea Research Part II, Topical Studies in Oceanography*, v. 53, p. 1420–1463.

- Hogarth, L.J., Driscoll, N.W., Babcock, J.M., and Orange, D.L., 2012, Transgressive deposits along the actively deforming Eel River Margin, Northern California: *Marine Geology*, v. 303–306, p. 99–114.
- Kieft, R.L., Hampson, G.J., Jackson, C.A.L., and Larsen, E., 2011, Stratigraphic architecture of a net-transgressive marginal- to shallow-marine succession: Upper Almond Formation, Rock Springs Uplift, Wyoming, U.S.A.: *Journal of Sedimentary Research*, v. 81, p. 513–533.
- Klotsko, S., Driscoll, N., Kent, G., and Brothers, D., 2015, Continental shelf morphology and stratigraphy offshore San Onofre, California: the interplay between rates of eustatic change and sediment supply: *Marine Geology*, v. 369, p. 116–126.
- Kraft, J.C., 1971, Sedimentary facies patterns and geologic history of a Holocene marine transgression: *Geological Society of America, Bulletin*, v. 82, p. 2131–2158.
- Labaune, C., Jouet, G., Berné, S., Gensous, B., Tesson, M., and Delpeint, A., 2005, Seismic stratigraphy of the Deglacial deposits of the Rhône prodelta and of the adjacent shelf: *Marine Geology*, v. 222–223, p. 299–311.
- Labaune, C., Tesson, M., and Gensous, B., 2008, Variability of the transgressive stacking pattern under environmental changes control: example from the Post-Glacial deposits of the Gulf of Lions inner-shelf, Mediterranean, France: *Continental Shelf Research*, v. 28, p. 1138–1152.
- Lambeck, K., and Chappell, J., 2001, Sea-level change through the last glacial cycle: *Science*, v. 292, p. 679–686.
- Lambeck, K., Esat, T.M., and Potter, E.-K., 2002, Links between climate and sea levels for the past three million years: *Nature*, v. 419, p. 199–206.
- Lambeck, K., Rouby, H., Purcell, A., Sun, Y., and Sambridge, M., 2014, Sea level and global ice volumes from the last glacial maximum to the Holocene: *National Academy of Sciences [USA], Proceedings*, v. 111, p. 15,296–15,303.
- Lantsch, H., Hanebuth, T.J.J., and Henrich, R., 2010, Sediment recycling and adjustment of deposition during deglacial drowning of a low-accumulation shelf (NW Iberia): *Continental Shelf Research*, v. 30, p. 1665–1679.
- Lebreiro, S.M., Voelker, A.H.L., Vizcaino, A., Abrantes, F.G., Alt-Epping, U., Jung, S., Thouveny, N., and Gràcia, E., 2009, Sediment instability on the Portuguese continental margin under abrupt glacial climate changes (last 60 kyr): *Quaternary Science Reviews*, v. 28, p. 3211–3223.
- Li, G., Li, P., Liu, Y., Qiao, L., Ma, Y., Xu, J., and Yang, Z., 2014, Sedimentary system response to the global sea level change in the East China Seas since the Last Glacial Maximum: *Earth-Science Reviews*, v. 139, p. 390–405.
- Liu, J.P., Milliman, J.D., Gao, S., and Cheng, P., 2004, Holocene development of the Yellow River's subaqueous delta, North Yellow Sea: *Marine Geology*, v. 209, p. 45–67.
- Lobo, F.J., Hernandez-Molina, F.J., Somoza, L., Rodero, J., Maldonado, A., and Barnolas, A., 2000, Patterns of bottom current flow deduced from dune asymmetries over the Gulf of Cadiz shelf (southwest Spain): *Marine Geology*, v. 164, p. 91–117.
- Lobo, F.J., Hernandez-Molina, F.J., and Diaz del Rio, V., 2001, The sedimentary record of the post-glacial transgression on the Gulf of Cadiz continental shelf (Southwest Spain): *Marine Geology*, v. 178, p. 171–195.

- Lobo, F.J., Sánchez, R., González, R., Dias, J.M.A., Hernández-Molina, F.J., Fernández-Salas, L.M., Díaz del Río, V., and Mendes, I., 2004, Contrasting styles of the Holocene highstand sedimentation and sediment dispersal systems in the northern shelf of the Gulf of Cadiz: *Continental Shelf Research*, v. 24, p. 461–482.
- Lobo, F.J., Dias, J.M.A., Hernandez-Molina, F.J., Gonzalez, R., Fernandez-Salas, L.M., and Diaz del Rio, V., 2005, Late Quaternary shelf-margin wedges and upper slope progradation in the Gulf of Cadiz margin (SW Iberian Peninsula), *in* Hodgson, D.M., and Flint, S.S., eds., *Submarine Slope Systems: Processes and Products*: Geological Society of London, Special Publication 244, p. 7–25.
- Lobo, F.J., Mendes, I., García, M., Reguera, M.I., Antón, L., Lebreiro, S.L., Van Rooij, D., Luján, M., Fernández-Puga, M.C., and Dias, J.M.A., 2015, A progradational pulse during the initial postglacial shelf drowning in the northern Gulf of Cadiz: Málaga, VIII Simposio sobre el Margen Ibérico Atlántico, p. 619–622.
- Lobo, F.J., García, M., Luján, M., Mendes, I., Reguera, M.I., and Van Rooij, D., 2018, Morphology of the last subaerial unconformity on a shelf: insights into transgressive ravinement and incised valley occurrence in the Gulf of Cádiz: *Geo-Marine Letters*, v. 38, p. 33–45.
- Maldonado, A., Rodero, J., Pallarés, L., Pérez, L., Somoza, L., Medialdea, T., Hernández-Molina, F.J., and Lobo, F.J., 2003, *Mapa Geológico de la Plataforma Continental Española y Zonas Adyacentes*, Cádiz: Instituto Geológico y Minero de España, Madrid, scale 1:200,000.
- Maselli, V., Hutton, E.W., Kettner, A.J., Syvitski, J.P.M., and Trincardi, F., 2011, High-frequency sea level and sediment supply fluctuations during Termination I: an integrated sequence-stratigraphy and modeling approach from the Adriatic Sea (Central Mediterranean): *Marine Geology*, v. 287, p. 54–70.
- Mesa-Fernández, J.M., Jiménez-Moreno, G., Rodrigo-Gámiz, M., García-Alix, A., Jiménez-Espejo, F.J., Martínez-Ruiz, F., Anderson, R.S., Camuera, J., and Ramos-Román, M.J., 2018, Vegetation and geochemical responses to Holocene rapid climate change in the Sierra Nevada (southeastern Iberia): the Laguna Hondera record: *Climate of the Past*, v. 14, p. 1687–1706.
- Mestdagh, T., Lobo, F.J., Llave, E., Hernández-Molina, F.J., and Van Rooij, D., 2019, Review of the late Quaternary stratigraphy of the northern Gulf of Cadiz continental margin: new insights into controlling factors and global implications: *Earth-Science Reviews*, v. 198, no. 102944.
- Mitchum, R.M., Jr., 1977, Seismic stratigraphy and global changes of sea level. Part 11: glossary of terms used in seismic stratigraphy, *in* Payton, C.E., ed., *Seismic Stratigraphy: Applications to Hydrocarbon Exploration*: American Association of Petroleum Geologists, Memoir 26, p. 205–212.
- Morales, J.A., 1997, Evolution and facies architecture of the mesotidal Guadiana River delta (SW Spain–Portugal): *Marine Geology*, v. 138, p. 127–148.
- Morellón, M., Aranbarri, J., Moreno, A., González-Sampériz, P., and Valero-Garcés, B.L., 2018, Early Holocene humidity patterns in the Iberian Peninsula reconstructed from lake, pollen and speleothem records: *Quaternary Science Reviews*, v. 181, p. 1–18.

- Nelson, C.H., Baraza, J., Maldonado, A., Rodero, J., Escutia, C., and Barber, J.H., Jr., 1999, Influence of the Atlantic inflow and Mediterranean outflow currents on Late Quaternary sedimentary facies of the Gulf of Cadiz continental margin: *Marine Geology*, v. 155, p. 99–129.
- Nicholls, R.J., Birkemeier, W.A., and Lee, G., 1998, Evaluation of depth of closure using data from Duck, NC, USA: *Marine Geology*, v. 148, p. 179–201.
- Nordfjord, S., Goff, J.A., Austin, J.A., and Duncan, L.S., 2009, Shallow stratigraphy and complex transgressive ravinement on the New Jersey middle and outer continental shelf: *Marine Geology*, v. 266, p. 232–243.
- Nummedal, D., and Swift, D.J.P., 1987, Transgressive stratigraphy at sequence-bounding unconformities: some principles derived from Holocene and Cretaceous examples, *in* Nummedal, D., Pilkey, O.H., and Howard, J.D., eds., *Sea-Level Fluctuation and Coastal Evolution*: SEPM, Special Publication 41, p. 241–260.
- Parsons, J.D., Friedrichs, C.T., Traykovski, P.A., Mohrig, D., Imran, J., Syvitski, J.P.M., Parker, G., Puig, P., Buttles, J.L., and García, M.H., 2007, The mechanics of marine sediment gravity flows, *in* Nittrouer, C.A., Austin, J.A., Field, M.E., Kravitz, J.H., Syvitski, J.P.M., and Wiberg, P.L., eds., *Continental Margin Sedimentation: International Association of Sedimentologist, Special Publication 37*, p. 275–337.
- Pellegrini, C., Maselli, V., Cattaneo, A., Piva, A., Ceregato, A., and Trincardi, F., 2015, Anatomy of a compound delta from the post-glacial transgressive record in the Adriatic Sea: *Marine Geology*, v. 362, p. 43–59.
- Peltier, W.R., and Fairbanks, R.G., 2006, Global glacial ice volume and last glacial maximum duration from an extended Barbados sea level record: *Quaternary Science Reviews*, v. 25, p. 3322–3337.
- Peltier, W.R., Argus, D.F., and Drummond, R., 2015, Space geodesy constrains ice age terminal deglaciation: the global ICE-6G_C (VM5a) model: *Journal of Geophysical Research, Solid Earth*, v. 119, p. 1–38.
- Penland, S., Boyd, R., and Suter, J.R., 1988, Transgressive depositional systems of the Mississippi delta plain: a model for barrier shoreline and shelf sand development: *Journal of Sedimentary Petrology*, v. 58, p. 932–949.
- Phillips, S.P., Howell, J.A., Hartley, A.J., and Chmielewska, M., 2020, Tidal estuarine deposits of the transgressive Naturita Formation (Dakota Sandstone): San Rafael Swell, Utah, U.S.A.: *Journal of Sedimentary Research*, v. 90, p. 777–795.
- Plomaritis, T.A., Benavente, J., Laiz, I., and Del Río, L., 2015, Variability in storm climate along the Gulf of Cadiz: the role of large scale atmospheric forcing and implications to coastal hazards: *Climate Dynamics*, v. 45, p. 2499–2514.
- Pretorius, L., Green, A.N., and Cooper, J.A.G., 2016, Submerged shoreline preservation and ravinement during rapid postglacial sea-level rise and subsequent “slowstand”: *Geological Society of America, Bulletin*, v. 128, p. 1059–1069.
- Pretorius, L., Green, A.N., Cooper, J.A.G., Hahn, A., and Zabel, M., 2019, Outer- to inner-shelf response to stepped sea-level rise: insights from incised valleys and submerged shorelines: *Marine Geology*, v. 416, 105979.

Puchała, R.J., Porbski, S.J., Śliwiński, W.R., and August, C.J., 2011, Pleistocene to Holocene transition in the central basin of the Gulf of Thailand, based on geoaoustic survey and radiocarbon ages: *Marine Geology*, v. 288, p. 103–111.

Rampino, M.R., and Sanders, J.E., 1980, Holocene transgression in south-central Long Island, New York: *Journal of Sedimentary Petrology*, v. 50, p. 1063–1080.

Rey, J., and Medialdea, T., 1989, Morfología y sedimentos recientes del margen continental de Andalucía Occidental, *in* Díaz del Olmo, F., and Rodríguez-Vidal, J., eds., *El Cuaternario de Andalucía Occidental: Asociación Española para el Estudio del Cuaternario, Monografías*, v. 1, p. 133–144.

Rodrigues, T., Grimalt, J.O., Abrantes, F.G., Flores, J.A., and Lebreiro, S.M., 2009, Holocene interdependences of changes in sea surface temperature, productivity, and fluvial inputs in the Iberian continental shelf (Tagus mud patch): *Geochemistry, Geophysics, Geosystems*, v. 10, no. Q07U06.

Rodrigues, T., Grimalt, J.O., Abrantes, F., Naughton, F., and Flores, J.-A., 2010, The last glacial–interglacial transition (LGIT) in the western mid-latitudes of the North Atlantic: abrupt sea surface temperature change and sea level implications: *Quaternary Science Reviews*, v. 29, p. 1853–1862.

Saito, Y., 1994, Shelf sequence and characteristic bounding surfaces in a wave-dominated setting: latest Pleistocene–Holocene examples from Northeast Japan: *Marine Geology*, v. 120, p. 105–127.

Sanders, J.E., and Kumar, N., 1975, Evidence of shoreface retreat and in-place “drowning” during Holocene submergence of barriers, shelf off Fire Island, New York: *Geological Society of America, Bulletin*, v. 86, p. 65–76.

Schattner, U., Lobo, F.J., López-Quirós, A., dos Passos Nascimento, J.L., and de Mahiques, M.M., 2020, What feeds shelf-edge clinofolds over margins deprived of adjacent land sources? An example from southeastern Brazil: *Basin Research*, v. 32, p. 293–301.

Shinn, Y.J., Chough, S.K., Kim, J.W., and Woo, J., 2007, Development of depositional systems in the southeastern yellow sea during the postglacial transgression: *Marine Geology*, v. 239, p. 59–82.

Siddall, M., Rohling, E.J., Almogi-Labin, A., Hemleben, C., Meischner, D., Schmelzer, L., and Smeed, D.A., 2003, Sea-level fluctuations during the last glacial cycle: *Nature*, v. 423, p. 853–858.

Spinelli, G.A., and Field, M.E., 2003, Controls of tectonics and sediment source locations on along-strike variations in transgressive deposits on the northern California margin: *Marine Geology*, v. 197, p. 35–47.

Stanford, J.D., Hemingway, R., Rohling, E.J., Challenor, P.G., Medina-Elizalde, M., and Lester, A.J., 2011, Sea-level probability for the last deglaciation: a statistical analysis of far-field records: *Global and Planetary Change*, v. 79, p. 193–203.

Stanley, D.J., 1995, A global sea-level curve for the late Quaternary: the impossible dream?: *Marine Geology*, v. 125, p. 1–6.

Storms, J.E.A., Weltje, G.J., Terra, G.J., Cattaneo, A., and Trincardi, F., 2008, Coastal dynamics under conditions of rapid sea-level rise: Late Pleistocene to Early Holocene

evolution of barrier-lagoon systems on the northern Adriatic shelf (Italy): *Quaternary Science Reviews*, v. 27, p. 1107–1123.

Stuiver, M., Reimer, P.J., and Reimer, R.W., 2021, CALIB 8.2: [WWW program]: <http://calib.org>, accessed 2021-7-20.

Swift, D.J.P., 1968, Coastal erosion and transgressive stratigraphy: *The Journal of Geology*, v. 76, p. 444–456.

Swift, D.J.P., 1975, Barrier-island genesis: evidence from the central Atlantic shelf, eastern U.S.A.: *Sedimentary Geology*, v. 14, p. 1–43.

Swift, D.J.P., 1976, Coastal sedimentation, *in* Stanley, D.J., and Swift, D.J.P., eds., *Marine Sediment Transport and Environmental Management*: New York, Wiley, p. 255–310.

Telford, R.J., Heegaard, E., and Birks, H.J.B., 2004, The intercept is a poor estimate of a calibrated radiocarbon age: *The Holocene*, v. 14, p. 296–298.

Thorndycraft, V.R., and Benito, G., 2006, The Holocene fluvial chronology of Spain: evidence from a newly compiled radiocarbon database: *Quaternary Science Reviews*, v. 25, p. 223–234.

Tortora, P., 1996, Depositional and erosional coastal processes during the last postglacial sea-level rise: an example from the central Tyrrhenian continental shelf (Italy): *Journal of Sedimentary Research*, v. 66, p. 391–405.

Trigo, R.M., and DaCamara, C.C., 2000, Circulation weather types and their influence on the precipitation regime in Portugal: *International Journal of Climatology*, v. 20, p. 1559–1581.

Trincardi, F., Correggiari, A., and Roveri, M., 1994, Late Quaternary transgressive record and deposition in a modern epicontinental shelf: the Adriatic semienclosed basin: *Geo-Marine Letters*, v. 14, p. 41–51.

Trincardi, F., Cattaneo, A., Asioli, A., Correggiari, A., and Langone, L., 1996, Stratigraphy of the Late-Quaternary deposits in the central Adriatic basin and the record of short term climatic events: *Istituto Italiano di Idrobiologia, Memorie*, v. 55, p. 39–70.

Vanney, J.-R., and Mougenot, D., 1981, La plate-forme continentale du Portugal et les provinces adjacentes, analyse géomorphologique: *Serviços Geológicos de Portugal, Memórias*, v. 28, 86 p.

Ximenes Neto, A.R., Morais, J.O., Paula, L.F.S., and Pinheiro, L.S., 2018, Transgressive deposits and morphological patterns in the equatorial Atlantic shallow shelf (Northeast Brazil): *Regional Studies in Marine Science*, v. 24, p. 212–224.

Zecchin, M., and Catuneanu, O., 2013, High-resolution sequence stratigraphy of clastic shelves I: units and bounding surfaces: *Marine Petroleum Geology*, v. 39, p. 1–25.

Zecchin, M., Gordini, E., and Ramella, R., 2015, Recognition of a drowned delta in the northern Adriatic Sea, Italy: stratigraphic characteristics and its significance in the frame of the early Holocene sea-level rise: *The Holocene*, v. 25, p. 1027–1038.

Received 30 September 2021; accepted 3 August 2022.

FIGURE CAPTIONS

Fig. 1.—The pattern of postglacial sea-level rise, with indication of major climatic events such as: Heinrich Event 1 (H1), the Bølling–Allerød warm period (B-A) and the Younger Dryas (YD) cold period. Timing of Melt-Water Pulses (MWP) 1A and 1B and the 8.2 ka

cooling event (in red) are also indicated. Sea-level curve is modified from Lambeck et al. (2014).

Fig. 2.—Examples of stratigraphic organization of postglacial transgressive deposits from various locations around the world. The relative position of each example is based on the prevailing sedimentation/erosion ratio in each setting (up and left where sedimentation is higher than erosion). **A)** Gulf of Lions, characterized by high rates of sediment supply (adapted from Gensous and Tesson 2003). **B)** Central Adriatic margin, also characterized by high rates of sediment supply. ES1, regional unconformity; S1 and S2, regional surfaces, each recording a specific interval of sea-level rise; Si, internal surface of erosion (adapted from Maselli et al. 2011). **C)** Offshore San Onofre, California characterized by a reduced amount of transgressive depositional bodies, possibly because of lower sediment inputs (adapted from Klotsko et al. 2015). **D)** East China Sea, where the transgressive architecture is strongly influenced by the hydrodynamic regime. TBL, transgressive boundary layer (adapted from Li et al. 2014). **E)** Durban shelf, eastern South Africa, characterized by the preferential development of barrier and backbarrier deposits (adapted from Pretorius et al. 2019). **F)** Continental shelf off New Jersey, characterized by a major role of transgressive ravinement. “R” horizon, a composite product of erosion, forms the base of three seismically recognized sedimentary deposits of latest Pleistocene–Holocene age older than the LGM. “T” horizon, the transgressive ravinement associated with Holocene sea-level rise (adapted from Nordfjord et al. 2009). Highstand systems tracts (HSTs) are represented in green, transgressive deposits are represented in orange. The different transgressive units are designated differently according to their sequential order in each location. mfs, maximum-flooding surface; TS, transgressive surface.

Fig. 3.—Location of the study area on the shelf offshore of the Guadiana River mouth, in the northern Gulf of Cadiz. **A)** Geographical location (inset rectangle) showing the main rivers and pathways of the main water masses and currents. **B)** Location of the seismic database on the shelf in the study area offshore of the Guadiana River mouth (EMODnet Bathymetry Consortium 2020). The location of Figures 4 to 7 is highlighted. **C)** Map showing the sediment distribution on the shelf in the study area offshore of the Guadiana River mouth (extracted from Gonzalez et al. 2004). The location of the sedimentological core stations and the location of Figures 9 to 12 are also marked.

Fig. 4.—Representative downdip cross-shelf (SSE–NNW-oriented) sub-bottom seismic profile showing: **A)** the general arrangement of backstepping seismic units and **B)** their interpretation offshore of the Guadiana River mouth. The color code and acronyms used in this work are also included. The location of the seismic section is indicated in Figure 3.

Fig. 5.—Representative sub-bottom profiles focusing on the Postglacial Transgressive Unit 4. **A)** W–E seismic line (up) and its interpretation (below). **B)** SSE–NNW seismic line (up) and its interpretation (below). Here, the important characteristics observed are: the clinofolds which compose the main body of PTU 4 (sub-unit 4a), mainly in the distal part of the unit; the channel features that characterize the proximal part of the body (sub-unit 4b); the transparent seismic facies that onlaps laterally to this body (sub-unit 4c); and the thin, and transparent facies, sheet-like body which integrates sub-unit 4d, where some superimposed undulations are observed. The location and penetration of sediment cores

LA-25-VC and LA-22-VC are also indicated. The location of the seismic sections is indicated in Figure 3. The color code and acronyms are indicated in Figure 4.

Fig. 6.—Representative sub-bottom profiles focusing on Postglacial Transgressive Units 3 and 2. **A)** W–E seismic line (above) and its interpretation (below). **B)** SSE–NNW seismic line (above) and its interpretation (below). Here, the remarked characteristics observed are: the low-angle clinofolds which compound the lower part of PTU3 (sub-unit 3a) and the two clinofolds bodies (with higher angles and dipping in opposite directions) that compound the most of PTU 2 (sub-units 2a1 and 2a2); the channel features with chaotic configuration that characterize the proximal part of the body (sub-unit 3b); the sub-unit 2d, which occurs over the proximal and central part of PTU 2, but is restricted only to the eastern sector; and the transparent seismic facies that onlaps laterally to sub-unit 2a2 (sub-unit 2c). The location and penetration of sediment cores LA-22-VC and LA-48-VC are also indicated. The location of the seismic sections is indicated in Figure 3. The color code and acronyms are indicated in Figure 4.

Fig. 7.—Representative sub-bottom profiles focusing on the Postglacial Transgressive Unit 1. **A)** W–E seismic line (above) and its interpretation (below). **B)** SSE–NNW seismic line (above) and its interpretation (below). Here, the remarked characteristics observed are: the three clinofold sub-units which form the main body of PTU 1 (i.e., sub-unit 1a1, 1a2, and 1a3); the sub-unit 1d, which occurs over the PTU 1; the transparent seismic facies that onlaps laterally to the main body of PTU 1 and is also lying over PTU 2 on the eastern sector (sub-unit 1c); and the incised-channel features located in the eastern sector, which contain parts of PTUs 2 and 3. The location and penetration of sediment core LA-18-VC are also indicated. The location of the seismic sections is indicated in Figure 3. The color code and acronyms are indicated in Figure 4.

Fig. 8.—Spatial distribution and thickness of the studied deposits. **A)** Distribution maps of the PTUs showing the location of the main Guadiana paleovalley, the coastline, and the shelf bathymetry. The position of Figure 8B–E is indicated by the inset rectangle. **B–D)** Isochores map showing the spatial distribution and thickness in TWTT (ms) of the studied seismic units: **B)** PTU 4, **C)** PTU 3, **D)** PTU 2, **E)** PTU 1. The shelf bathymetry and the position of sub-bottom seismic lines are also represented.

Fig. 9.—Photography, schematic sediment facies, and lithological description, control age points, density log, and magnetic susceptibility logs of sediment core LA-25-VC, characterizing seismic unit PTU 4. **A)** Homogeneous mud (facies 3). **B, C)** Silty sand mixed with highly fragmented bioclasts of bivalves, *Turritella* and *Ostrea* up to 2 cm in length (facies 2). **D)** Massive medium to fine sand with mottling related to organic matter. **E)** Fine to medium sand with some silt laminae. **F, G)** Massive sands (facies 1).

Fig. 10.—Photography, schematic facies, lithological description, control age points, density log, and magnetic susceptibility logs of sediment core LA-22-VC, characterizing seismic unit PTU 3. **A)** Muddy facies (Facies 3) showing a large well-preserved 3-cm-long bivalve shell. **B)** Silty sand of facies 2 with 1-cm-long bivalve shell fragments (facies 2). **C)** Medium sand of facies 2 including a high amount of fragmented bioclasts of bivalves and *Turritella* and silt nodules. **D)** Medium sand including fragmented bioclasts like bivalves and *Turritella* up to 3 cm in length. **E)** Massive medium sand

containing a large 5 cm bivalve shell and *Dentalium*. **F**) Bioturbation in fine to medium sand. **G**) Massive fine sand including a large bivalve shell fragment.

Fig. 11.—Photography, schematic facies, lithological description, control age points, density log, and magnetic susceptibility logs of sediment core LA-48-VC, characterizing seismic unit PTU 2. **A**) Silts (facies 3) containing a large well-preserved 5 cm *Ostrea* shell. **B**) Mixture of medium to coarse sand with scattered large bivalve and *Turritella* shell fragments up 2 cm in length. **C**) Medium to fine sand (facies 1). **D**) Bioclastic layer hosted in a fine sand interval. **E**) Massive fine sand of facies 1 including a large bivalve shell. **F**, **G**) Massive medium sand.

Fig. 12.—Photography, schematic facies, lithological description, control age points, density log, and magnetic susceptibility logs of sediment core LA-18-VC, characterizing seismic unit PTU 1. **A**) Massive fine sand of facies 1. **B**) Medium sand of facies 2 with abundant fragmented bioclasts including *Pecten*. **C**) Erosional surface between fine sandy (facies 1) and silty facies (facies 2). **D**) Fine to medium sand of facies 1 showing some silt laminations. **E**) Massive fine sand of facies 1 including some granule- to pebble-size shell fragments. **F**) Sandy gravels with bivalves and gastropods including a large shell. **G**) Massive fine sand of facies 1.

Fig. 13.—Schematic block diagrams and cross sections showing the model of sedimentary evolution proposed for the formation of a generic transgressive deposit associated with the postglacial retreat of the Guadiana River mouth. Dashed lines and blue arrows show the position of sea level in the previous phases. **A**) Phase of clinof orm body development (i.e., sub-units a), representing the establishment of a coastal regime, during which shallow-water, coarse-grained river-dominated deltas formed. **B**) Phase of delta-top distributary-channel formation following construction of transgressive delta. **C**) Phase of infilling of erosional channels (i.e., sub-units b) over the proximal areas of the clinof orms and fine-grained sediment export to construct distal sediment sheets (i.e., sub-units c). **D**) Final evolutionary phase of each transgressive deposit, characterized by shoreface reworking (i.e., sub-units d) of the previous fluvio-deltaic depositional system.

Fig. 14.—Proposed chronology of transgressive seismic units (including ages of PTU 5 after Lobo et al. 2015) and correlation with the postglacial sea-level pattern (rate of sea-level change above and amplitude of sea-level change below). The major climatic events include: Heinrich Event 1 (H1), the Bølling–Allerød warm period (B-A) and the Younger Dryas (YD) cold period, as well as the timing of Melt-Water Pulses (MWP) 1A and 1B and the 8.2 ka cooling event (in red). Plotted ages are named taking into account the coring site, the coring technique (VC stands for vibrocoring), and the name of the seismic unit in which the samples were taken. The estimated water-depth locations of the Gulf of Cadiz transgressive clinof orms in relation to coeval sea levels are also indicated.

TABLE CAPTION

TABLE 3.—Summary table including the seismic facies, configuration, boundaries, and acronyms for each seismic sub-unit identified in this study.

Figure 1

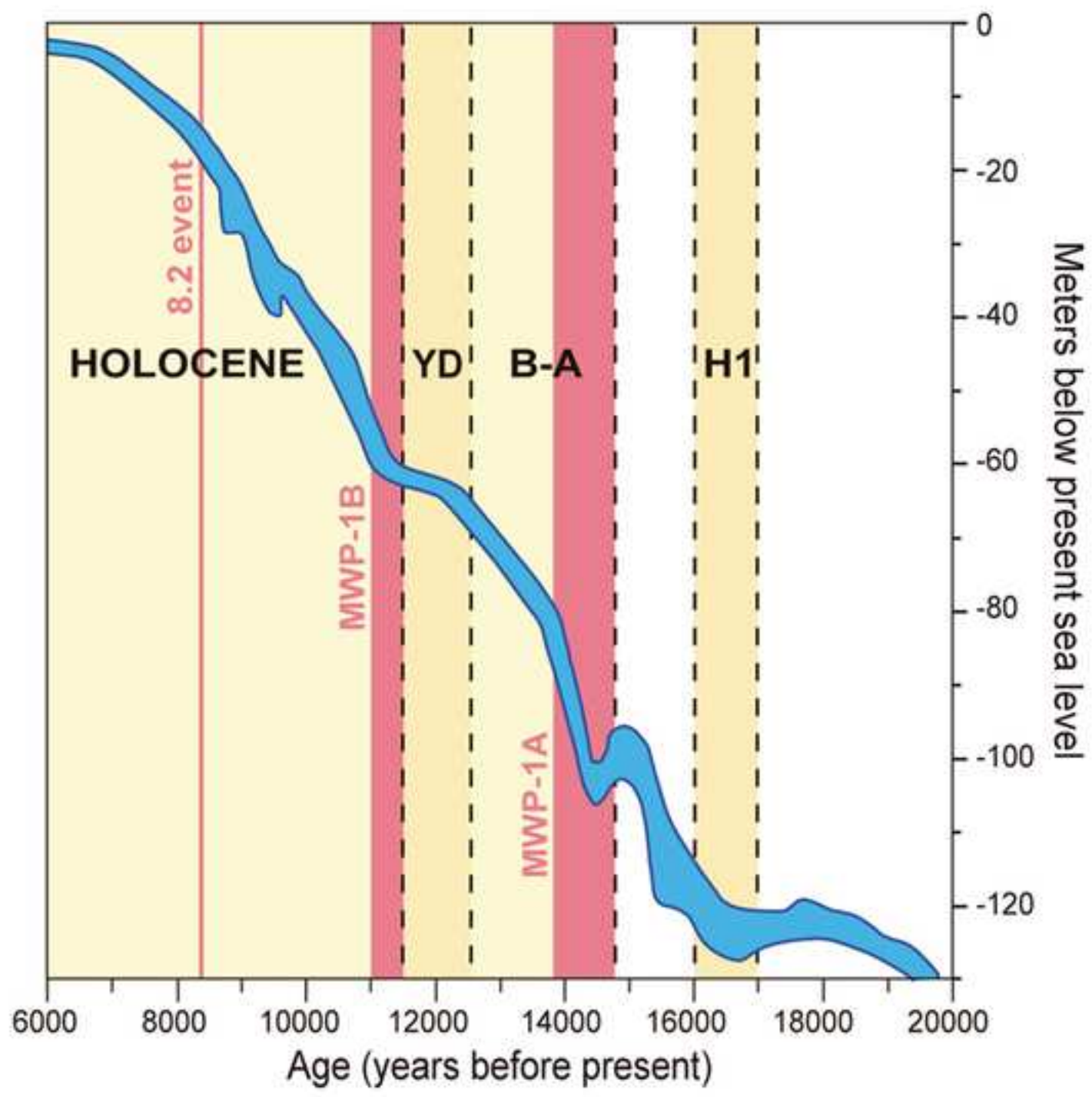


Figure 2

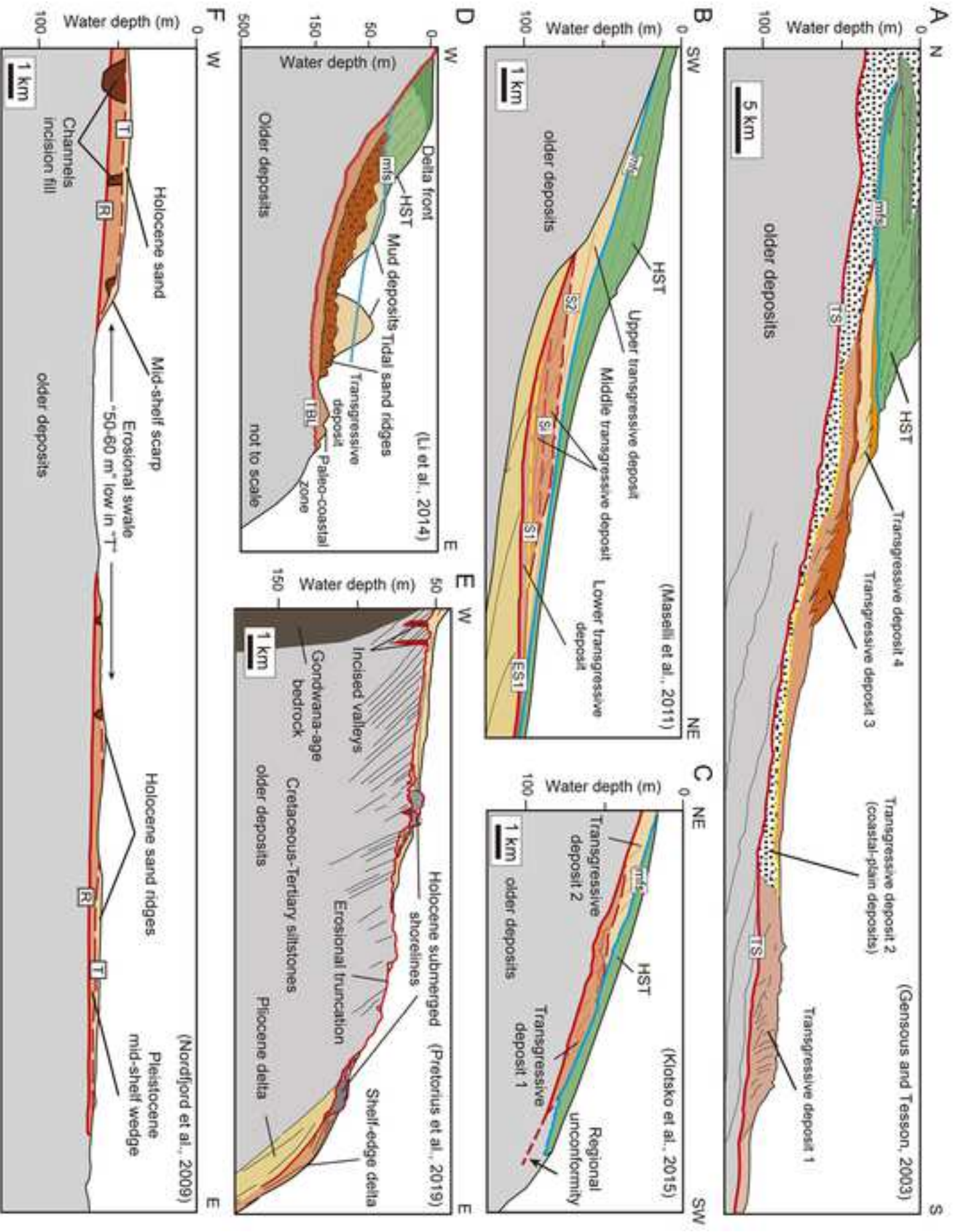


Figure 3

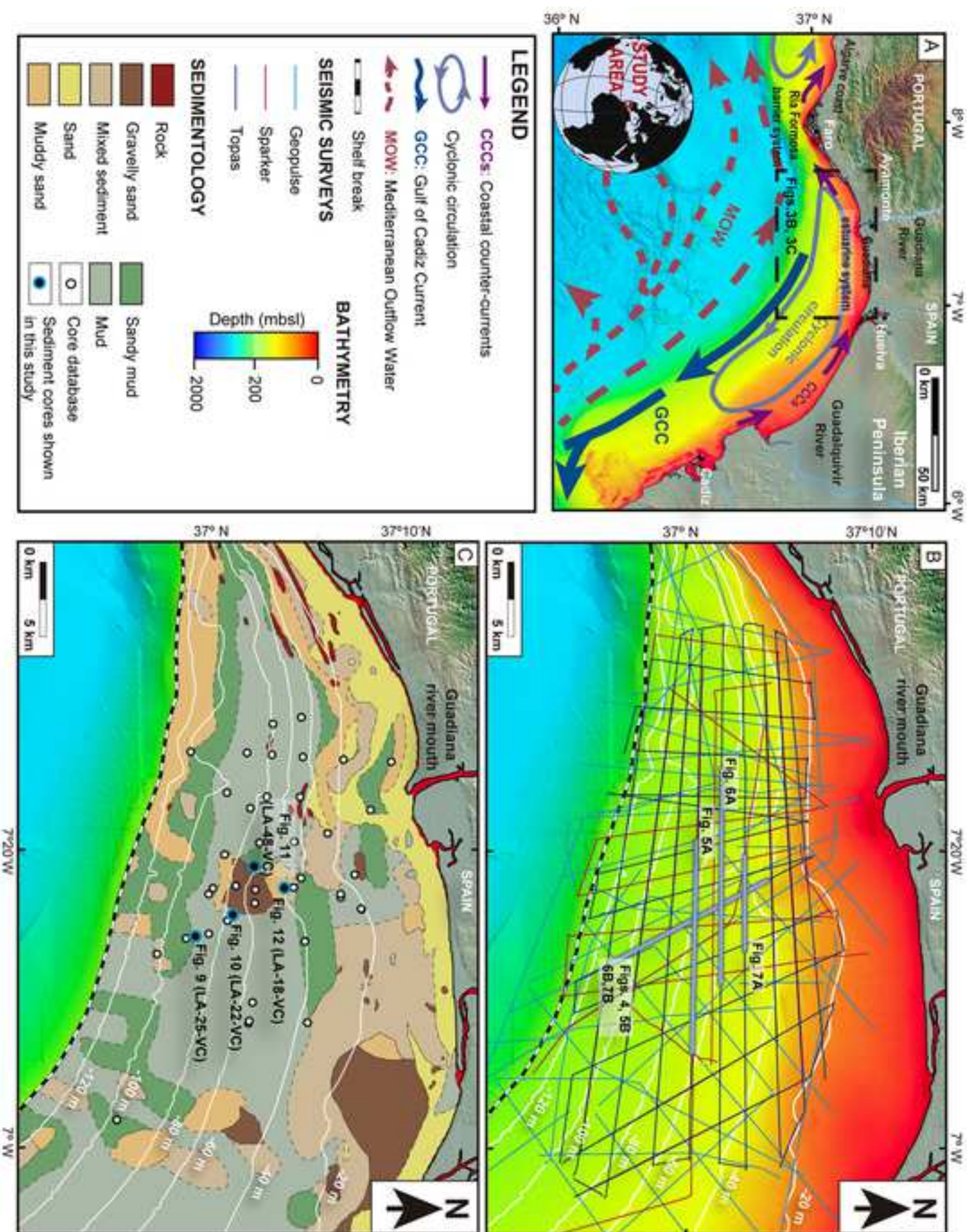


Figure 4

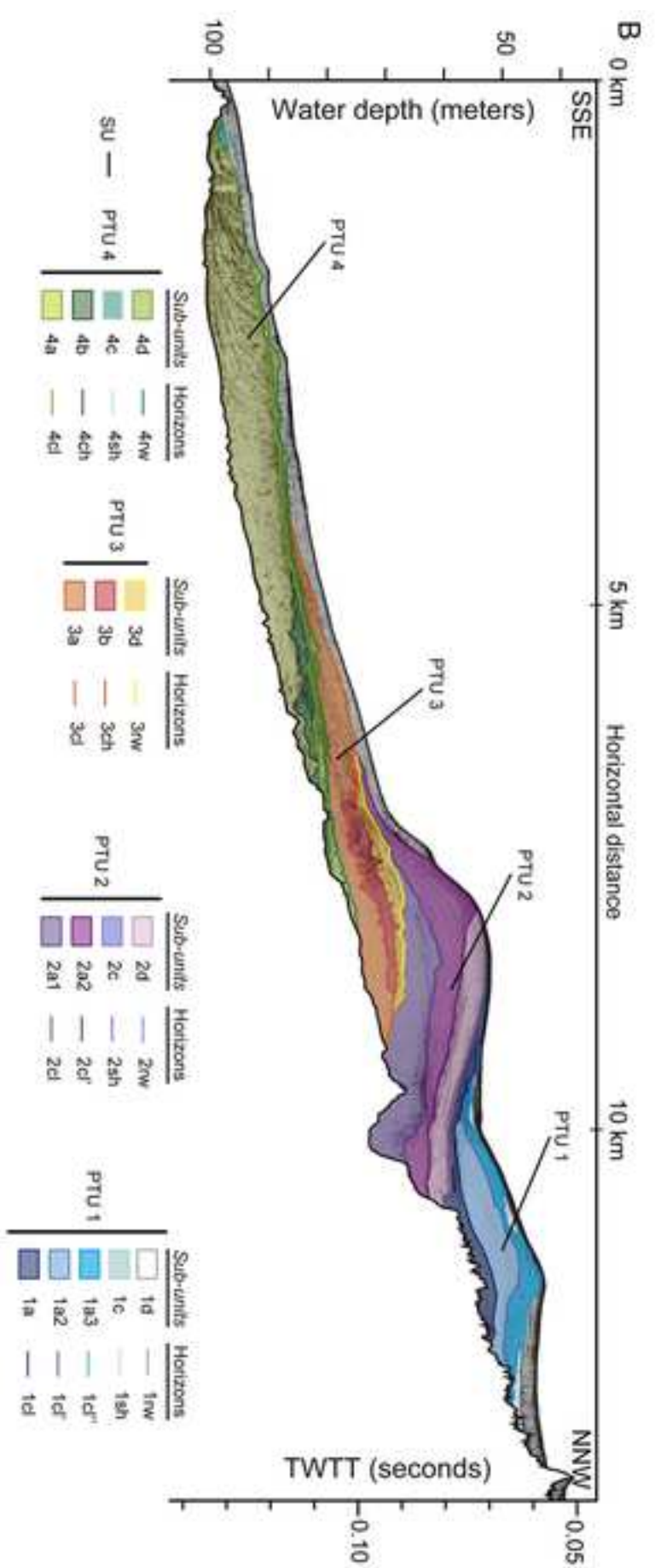
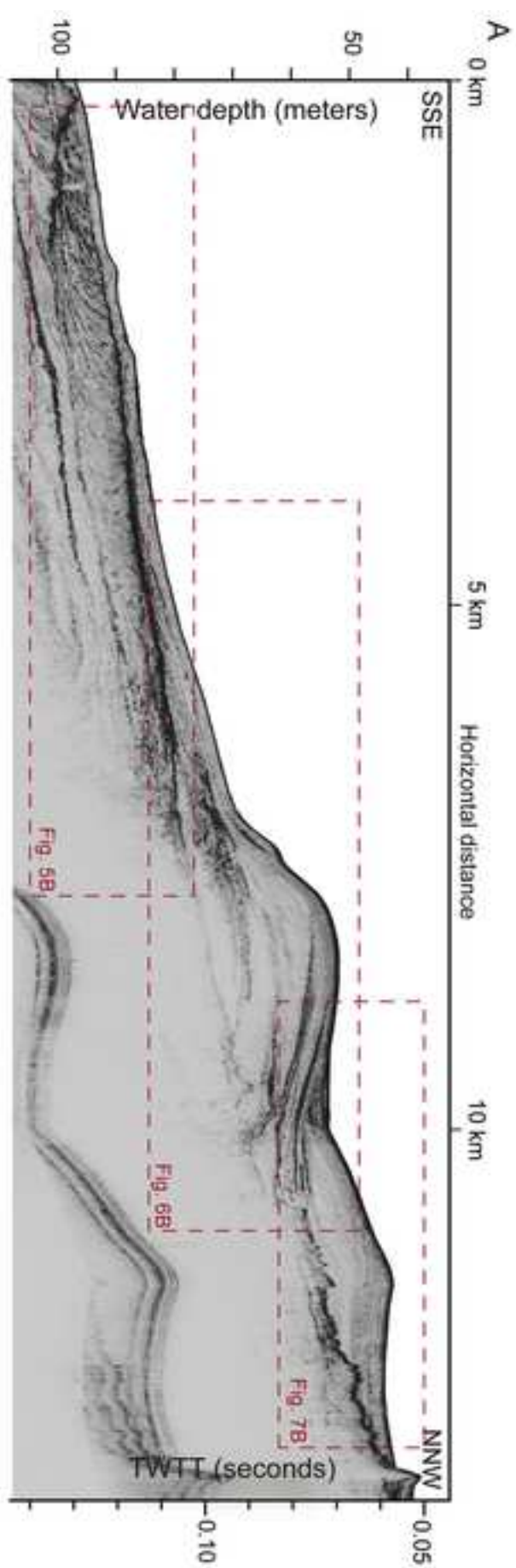
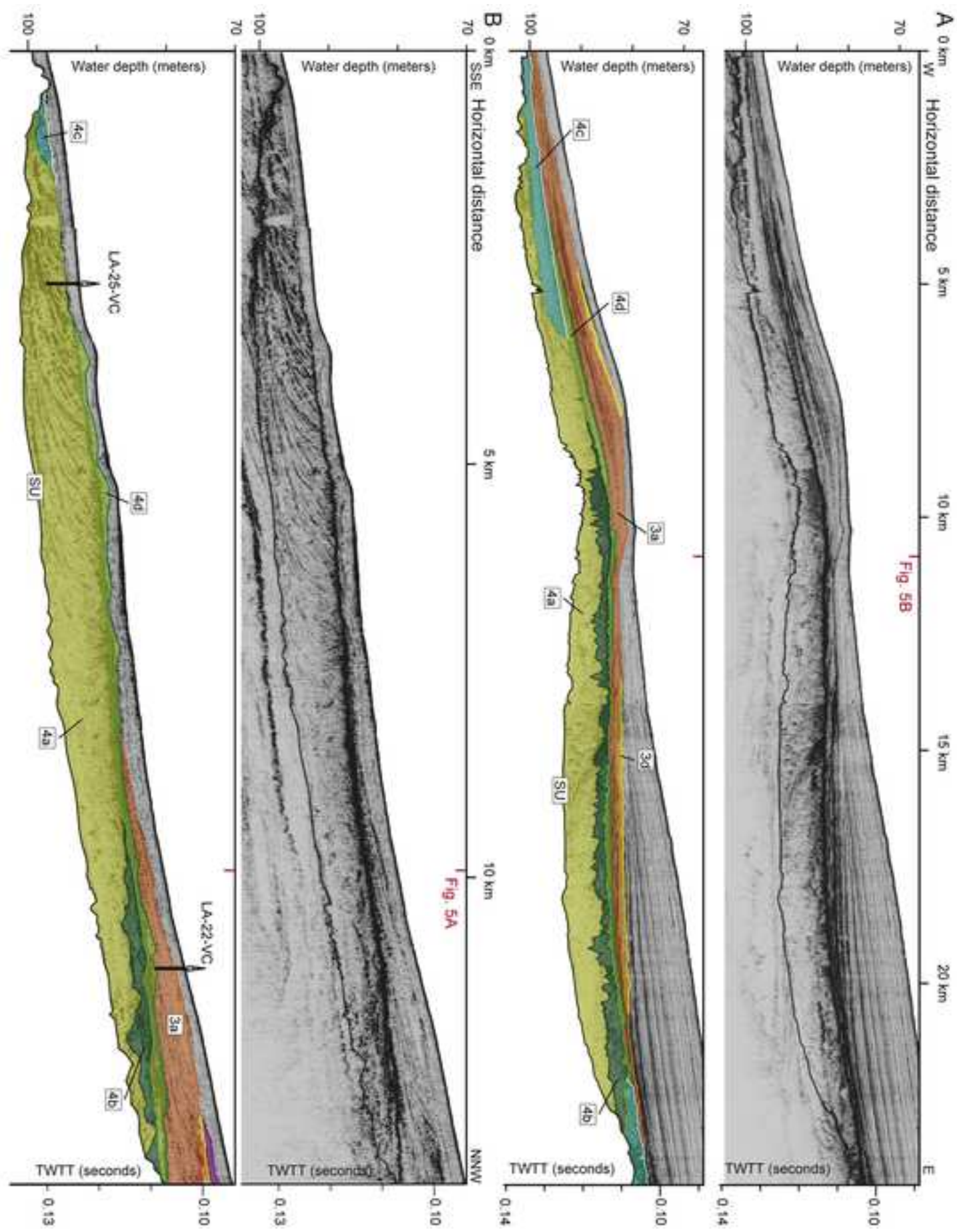


Figure 5



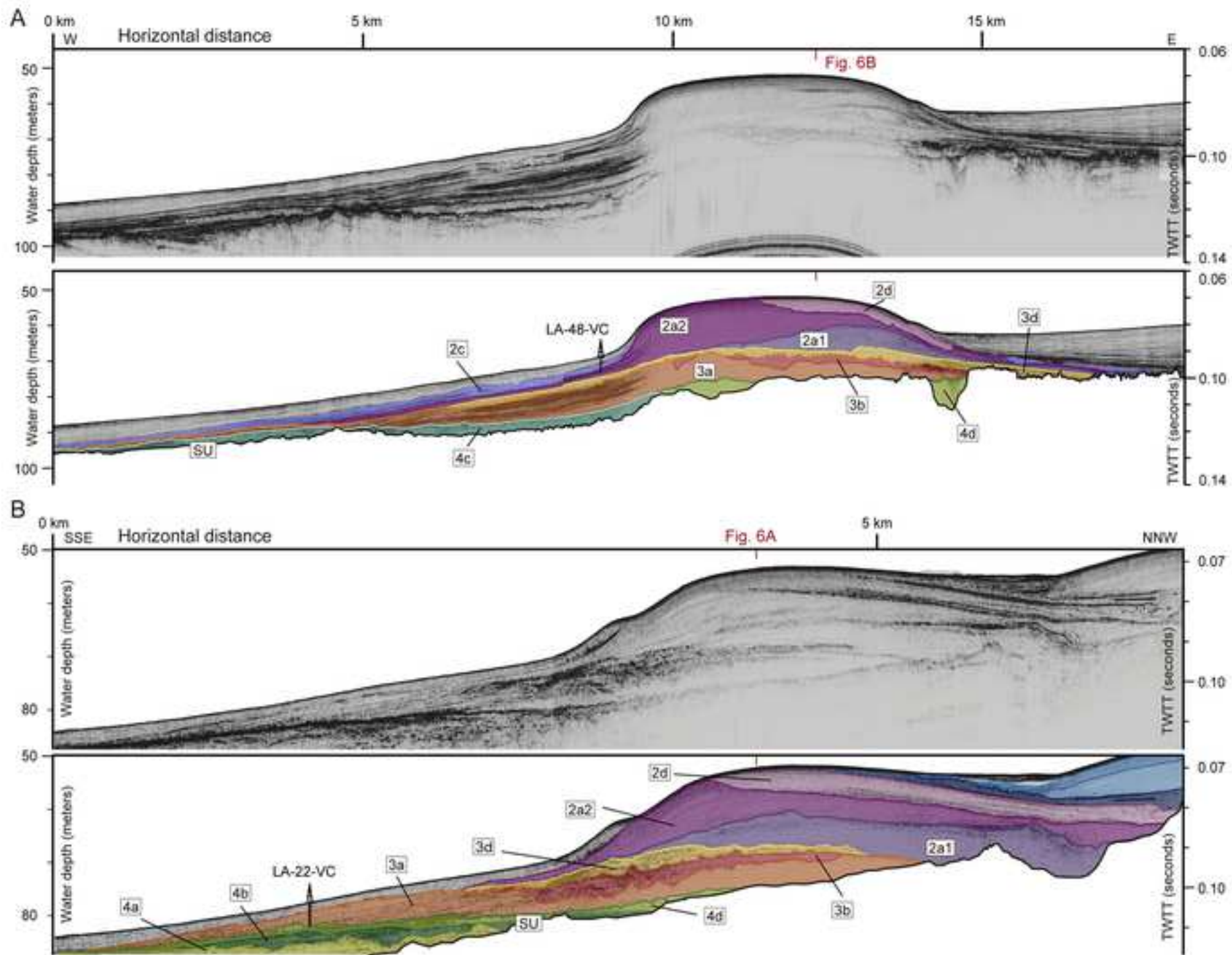


Figure 7

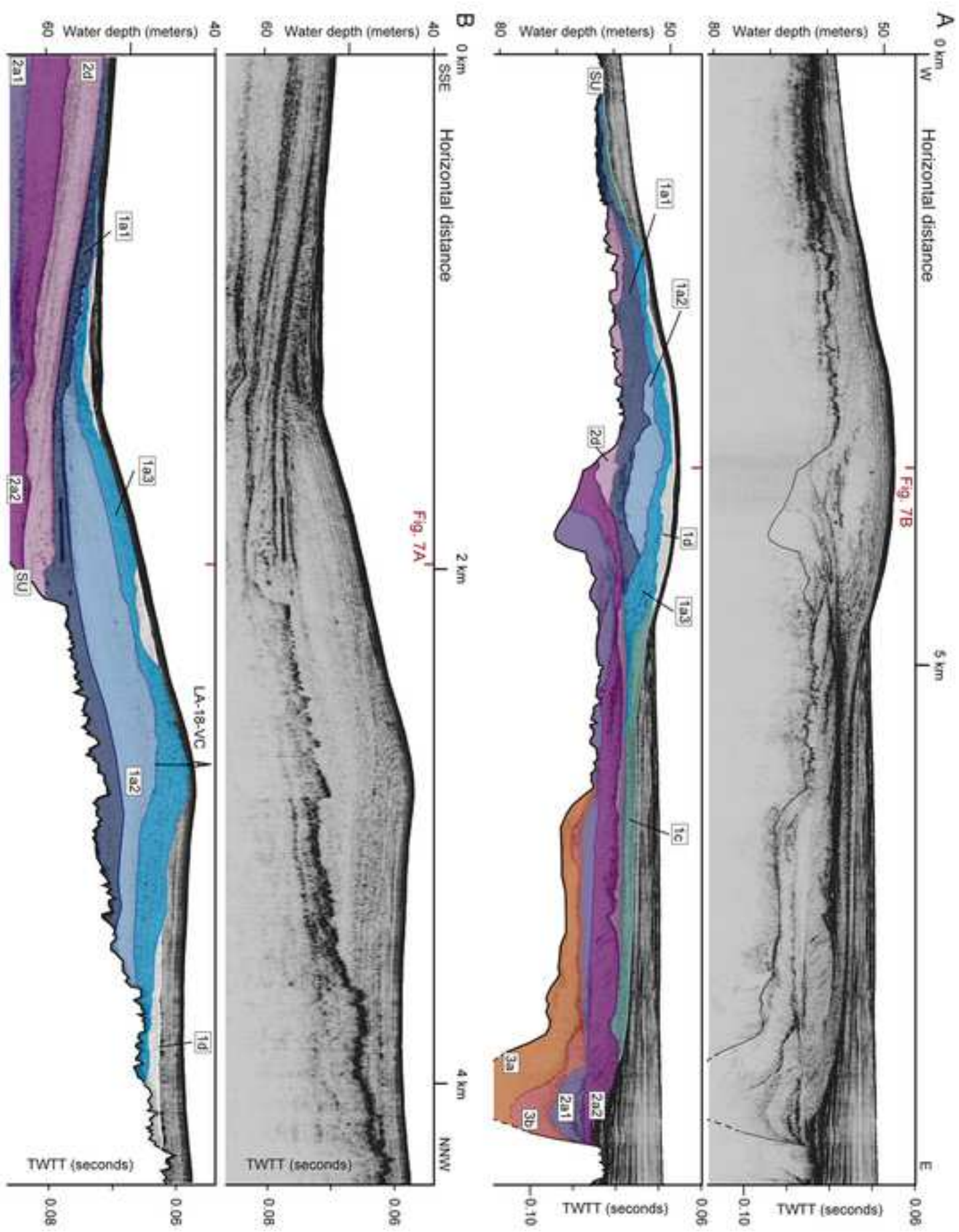


Figure 8

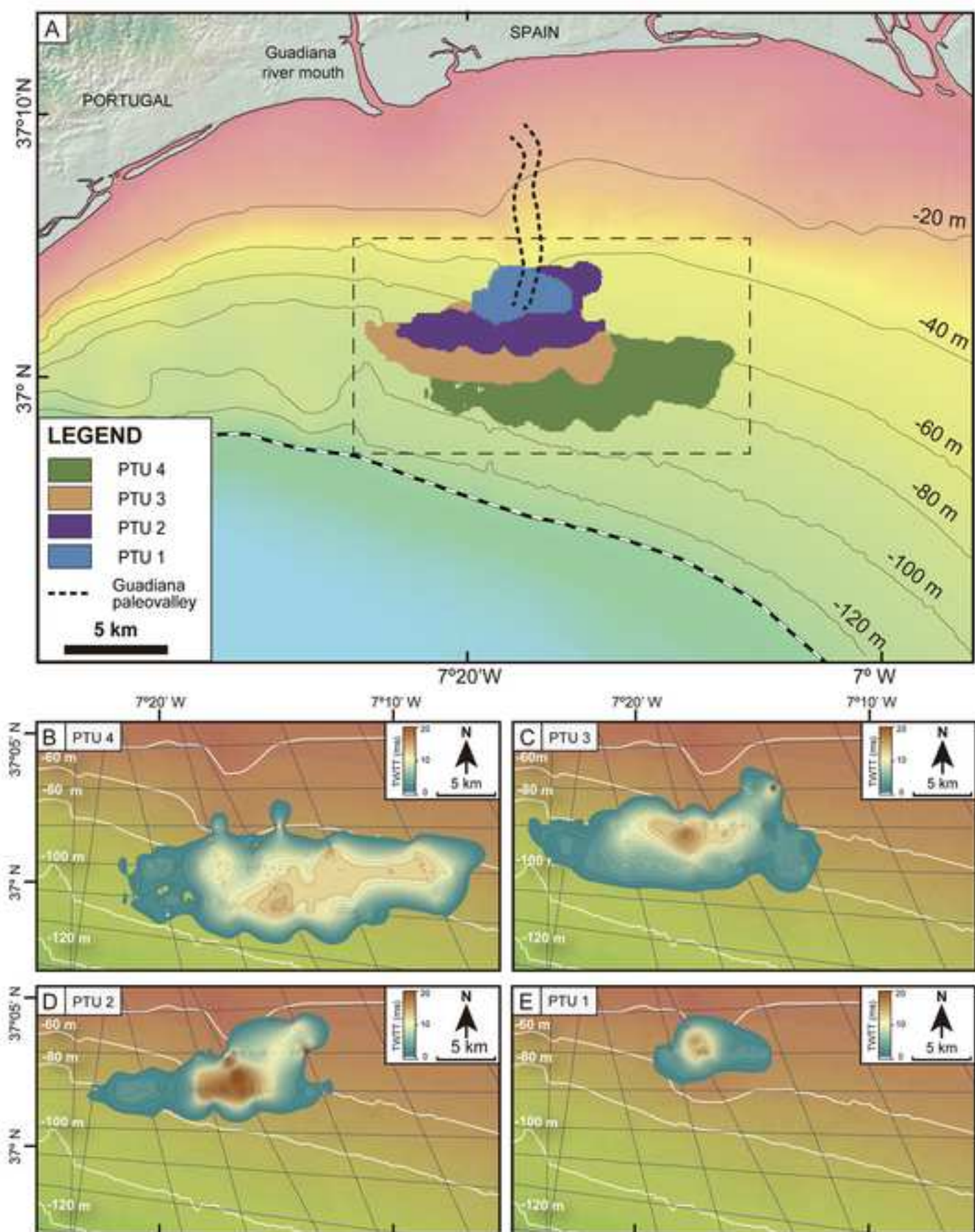


Figure 9

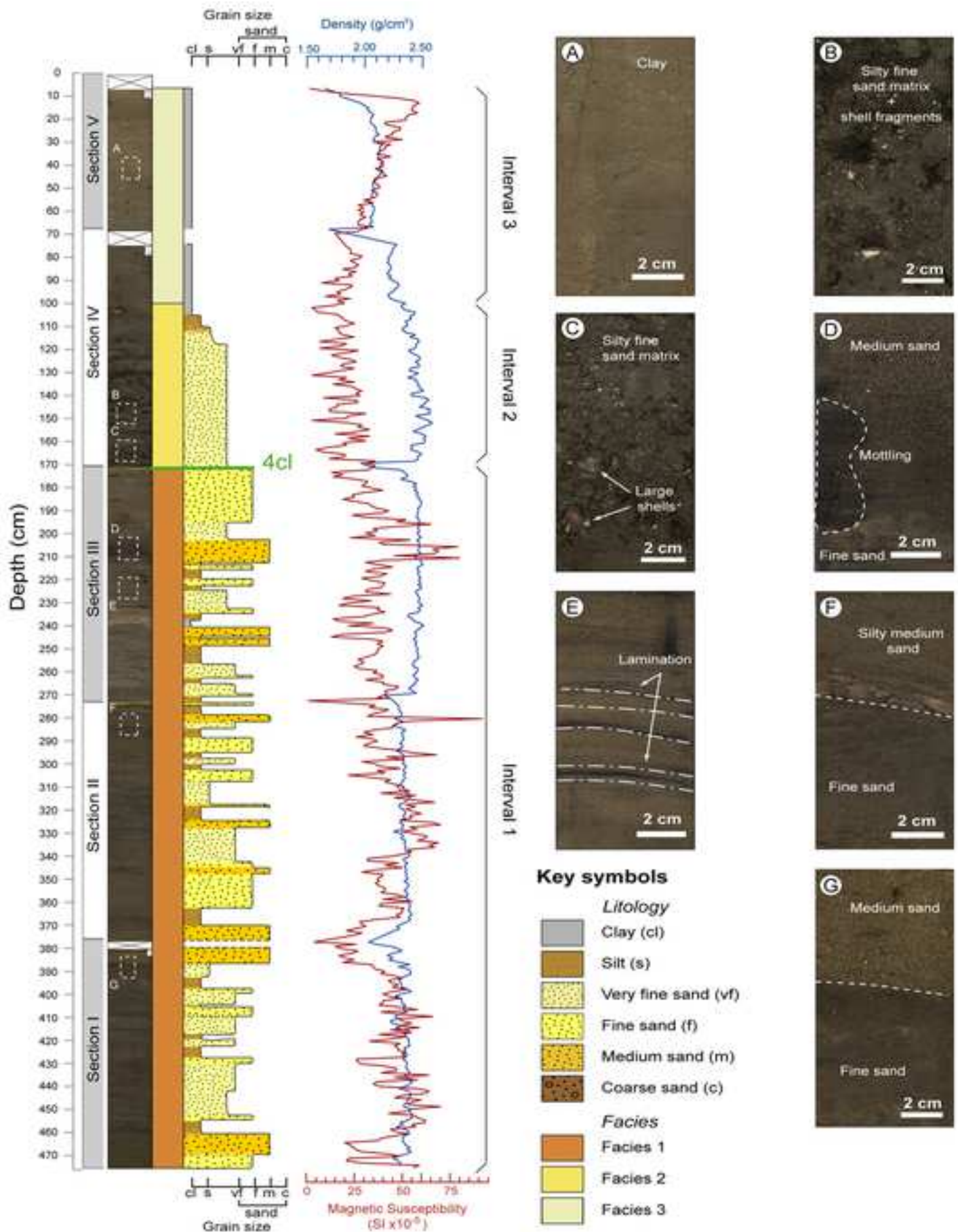
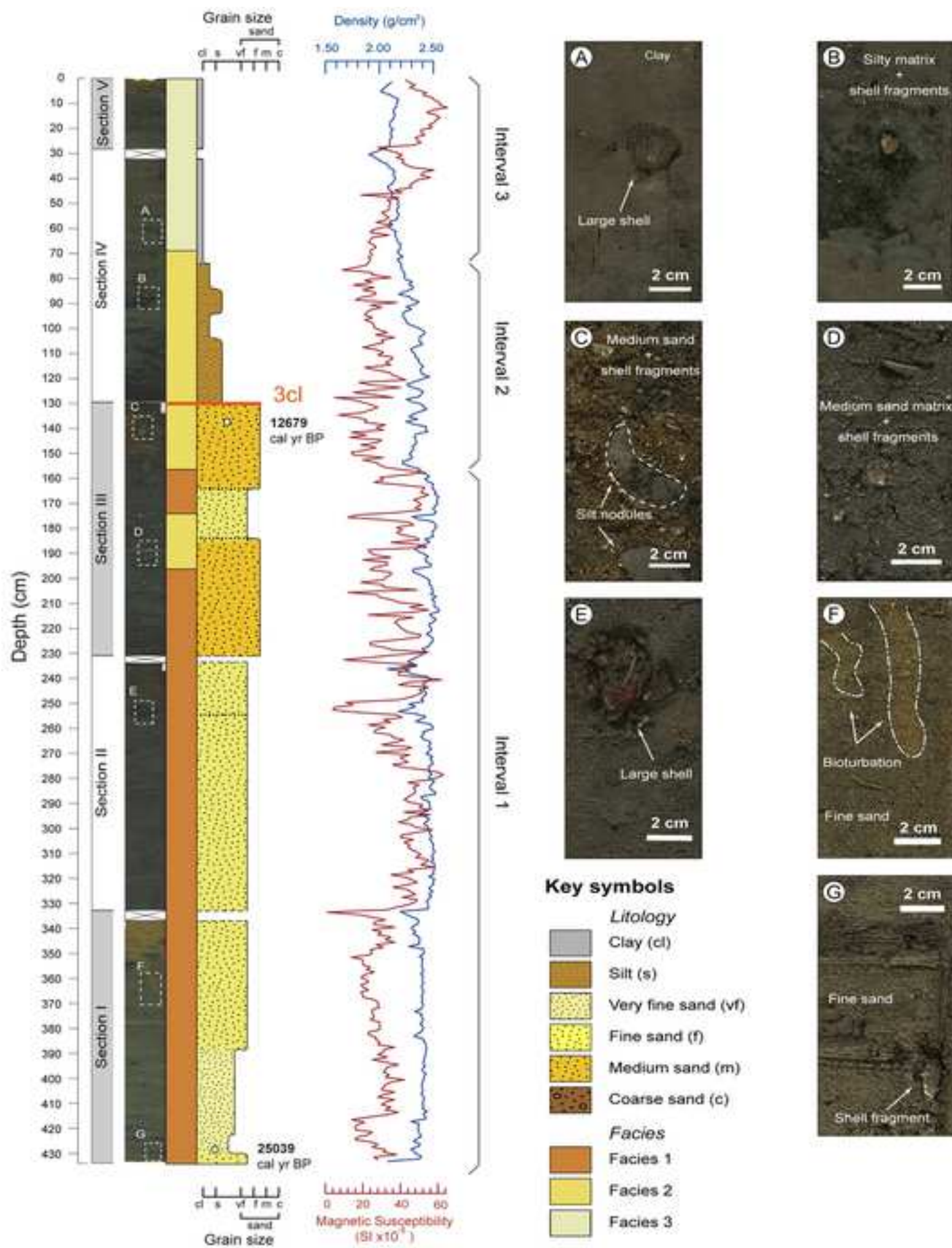
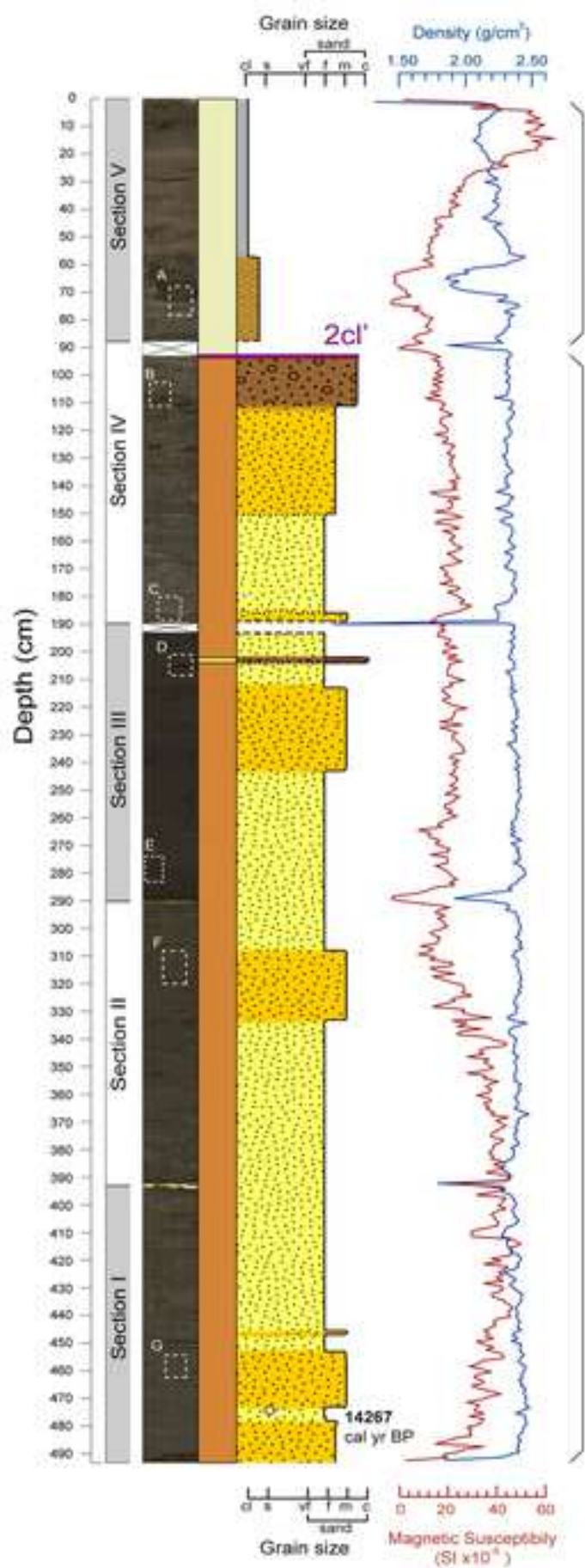


Figure 10



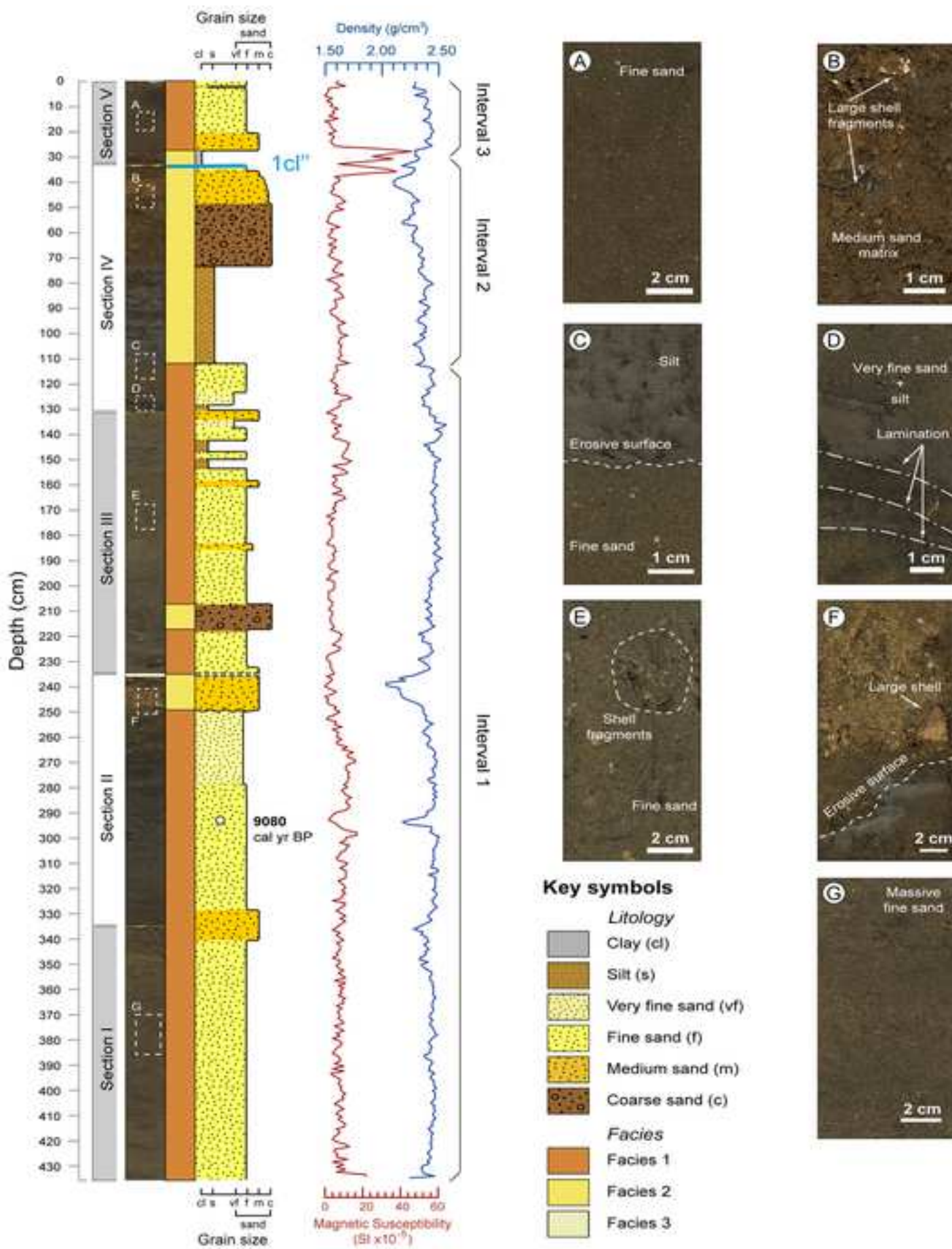


Key symbols

- Litology*
- Clay (cl)
 - Silt (s)
 - Very fine sand (vf)
 - Fine sand (f)
 - Medium sand (m)
 - Coarse sand (c)
- Facies*
- Facies 1
 - Facies 2
 - Facies 3



Figure 12



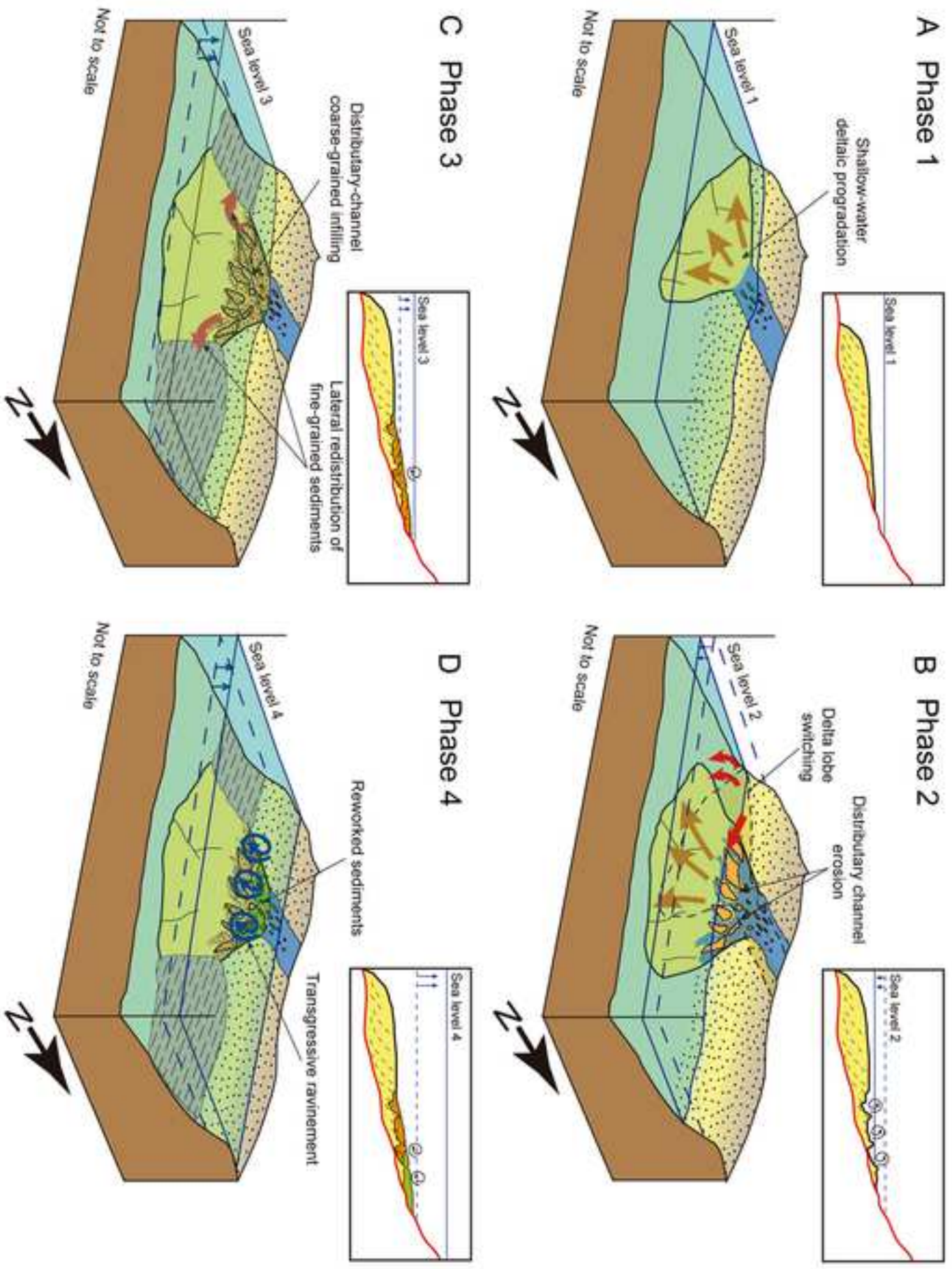


Figure 14

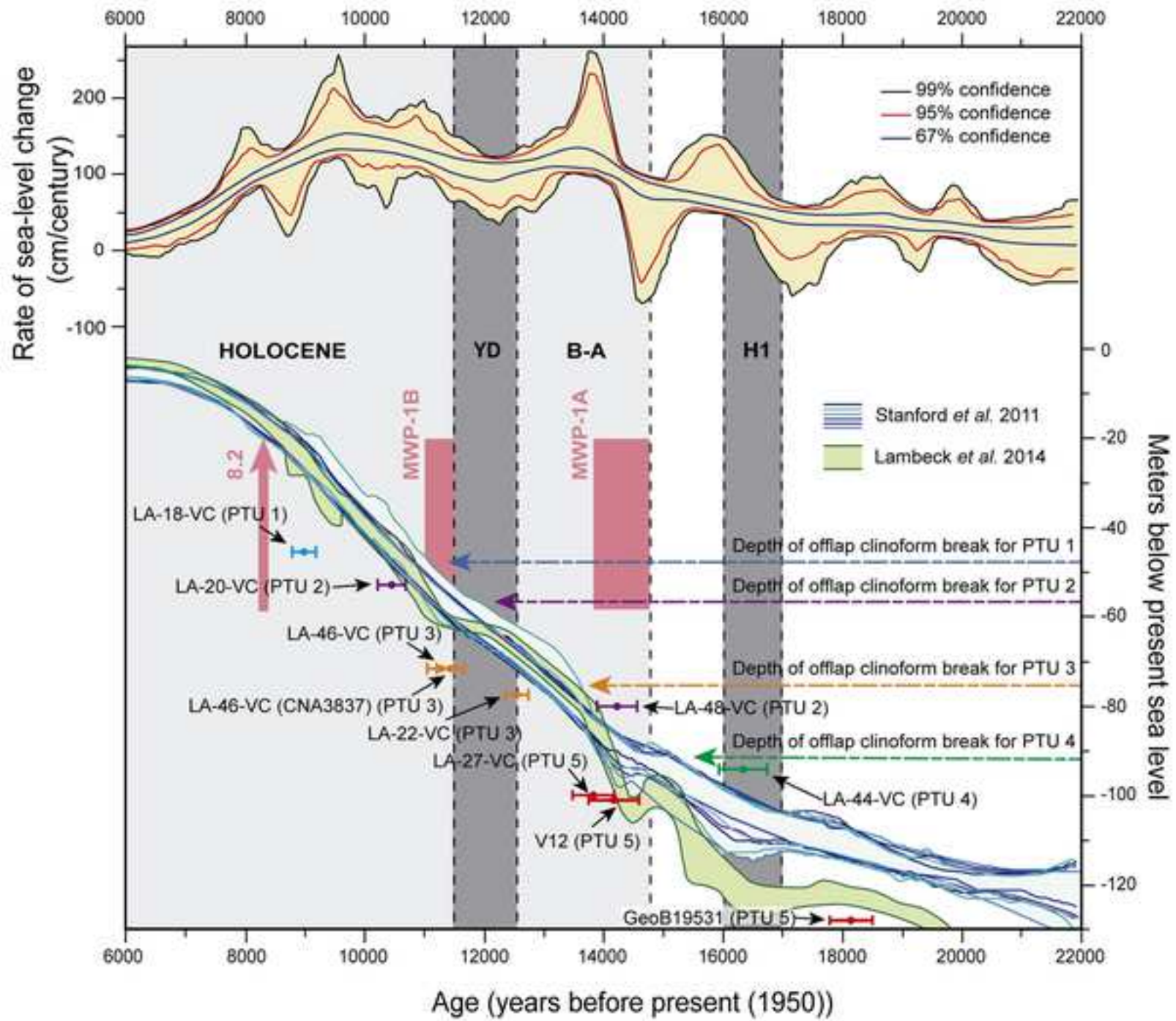


TABLE 1.—Summary table of the studied sediment vibrocores, including coordinates, length, and the water depths in which they were obtained.

Unit	Core ID	Geographic Coordinates		Water depth (m)	Core length (cm)
		Latitude (N)	Longitude (W)		
PTU4	LA-44-VC	36° 59' 115	7° 17' 429	89	413.6
	LA-25-VC	36° 58' 386	7° 14' 697	95	483.2
PTU 3	LA-22-VC	37° 00' 379	7° 15' 926	77	444.3
	LA-46-VC	37° 00' 596	7° 17' 899	67	399.7
PTU2	LA-48-VC	37° 01' 560	7° 19' 104	70.4	494.8
	LA-20-VC	37° 01' 599	7° 16' 721	52	70
PTU1	LA-18-VC	37° 03' 226	7° 17' 736	41	437.7

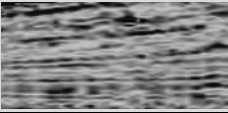



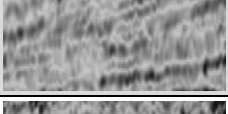
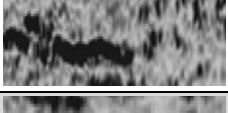

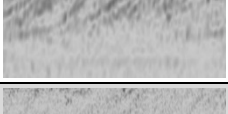


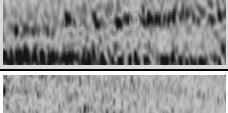
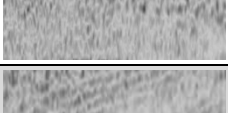
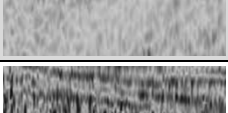
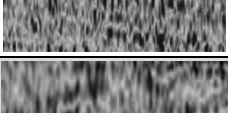
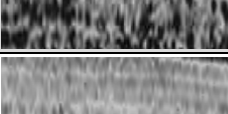

TABLE 2.—AMS radiocarbon data obtained on benthic foraminifera and shells in the studied sediment cores. Ages written in *italics* point out the anomalous results that provide ages older than expected.

Unit	Core ID	Core Section	Sampling Depth in Core Section (cm)	Depth in Core (cm)	Lab. no.	Sample Material	$\delta^{13}\text{C}$ ‰	pMC	Conventional Age ^{14}C BP	cal yr BP (68.3%, 1s)	cal yr BP (95.4%, 2s)	Median Probability ^a	Relative Area under Probability Distribution 1.000 ^c
PTU1	LA-18-VC	II	62	292.3	Poz-78917	Fragile valve	4.8 ± 1	34.21 ± 0.21	8620 ± 50	8985–9179	8885–9284	9080	1
PTU2	LA-20-VC	I	10	8.5	Poz-78920	Shells	3.3 ± 0.6	93.11 ± 0.32	575 ± 30	<i>post 1950^b</i>	<i>post 1950^b</i>		
		I	48	46	Poz-78921	Shell alone	-2.2 ± 0.7	29.69 ± 0.19	9760 ± 60	10409–10643	10273–10739	10521	1
	LA-48-VC	I	88	475.3	Poz-78703	Foraminifera	-5 ± 0.6	20.40 ± 0.18	12740 ± 70	<i>14080–14410</i>	<i>13983–14653</i>	<i>14267</i>	<i>1 (68.3%) & 0.992 (95.4%)</i>
PTU3	LA-46-VC	III	93	199.5	Poz-78916	Shell valves	-0.5 ± 0.7	27.7 ± 0.19	10310 ± 60	11180–11387	11097–11554	11291	1
		III	93	199.5	CNA3837	Shell valves	-1.18 ± 1.5	27.26 ± 0.13	10441 ± 38	11347–11586	11255–11695	11469	1
	LA-22-VC	III	4	136.3	Poz-78922	Shell valves	0.7 ± 0.4	24.42 ± 0.18	11330 ± 60	12604–12747	12448–12830	12679	1
		I	92	428.9	Poz-78704	Foraminifera	-9.7 ± 0.6	6.73 ± 0.13	21670 ± 160	<i>24817–25256</i>	<i>24591–25496</i>	<i>25039</i>	<i>1</i>
PTU4	LA-44-VC	II	16	226.4	Poz-78923	Shell alone	-1.1 ± 0.5	17.04 ± 0.15	14210 ± 80	<i>16202–16503</i>	<i>15967–16770</i>	<i>16355</i>	<i>1</i>

^a Online program Calib.8.2, which uses the marine20.14c calibration dataset recommended for marine samples limited to 603-50,788 ^{14}C year BP (Heaton et al. 2020; Stuiver et al. 2021)

^b No valid radiocarbon age between 603 and 50779 yrs BP for this calibration curve

^c Heaton et al. 2020

Unit	Sub-unit	Aspect	Seismic Configuration	Lower Boundary	Upper Boundary
PTU4	4a		Amplitude: High to medium Configuration: Clinofolds Geometry: Wedge	Seismic Horizons: SU Termination: Downlap	Seismic Horizons: 4cl, 4ch Termination: Toplap/ Concordance/Erosion
	4b		Amplitude: Medium to low Configuration: Transparent to chaotic with scattered internal reflections Geometry: Channel-like infilling	Seismic Horizons: 4ch, SU Termination: Onlap/Downlap	Seismic Horizons: 4cl Termination: Toplap/Erosion
	4c		Amplitude: Low Configuration: Transparent with scattered internal reflections Geometry: Sheet-like	Seismic Horizons: SU, 4cl Termination: Downlap, Onlap	Seismic Horizons: 4sh, Termination: Toplap
	4d		Amplitude: Very low Configuration: Transparent Geometry: Sheet-like	Seismic Horizons: 4cl, 4sh Termination: Concordance	Seismic Horizons: 4rw Termination: Concordance/Erosion
PTU3	3a		Amplitude: High to medium Configuration: Clinofolds Geometry: Wedge	Seismic Horizons: SU, 4rw Termination: Downlap	Seismic Horizons: 3cl, 3ch Termination: Toplap/ Erosion
	3b		Amplitude: Medium Configuration: Chaotic Geometry: Channel-like infilling	Seismic Horizons: 3ch Termination: Erosion/Onlap/Downlap	Seismic Horizons: 3cl Termination: Toplap/Erosion
	3d		Amplitude: Low Configuration: Chaotic/Transparent Geometry: Sheet-like	Seismic Horizons: 3cl, SU Termination: Concordance	Seismic Horizons: 3rw, Termination: Concordance/Erosion
PTU2	2a1		Amplitude: Medium to low Configuration: Clinofolds Geometry: Wedge	Seismic Horizons: SU, 3rw Termination: Downlap/Onlap	Seismic Horizons: 2cl Termination: Toplap/ Concordance/Erosion
	2a2		Amplitude: Low Configuration: Clinofolds Geometry: Wedge/Mound	Seismic Horizons: SU, 3rw, 3cl, 2cl Termination: Downlap	Seismic Horizons: 2cl' Termination: Toplap/ Erosion
	2c		Amplitude: Very low Configuration: Transparent with scattered internal reflections Geometry: Sheet-like	Seismic Horizons: 2cl' Termination: Downlap, Onlap	Seismic Horizons: 2sh, Termination: Toplap
	2d		Amplitude: Low Configuration: Transparent with some internal reflections Geometry: Sheet-like	Seismic Horizons: 3cl, 2cl', SU Termination: Concordance	Seismic Horizons: 2rw Termination: Concordance/Erosion
PTU1	1a1		Amplitude: Low Configuration: Transparent with some internal reflections Geometry: Wedge	Seismic Horizons: SU, 2rw Termination: Downlap/ Onlap	Seismic Horizons: 2cl Termination: Toplap/ Concordance/Erosion
	1a2		Amplitude: Low-very low Configuration: Transparent with scattered internal reflections Geometry: Wedge/Mound	Seismic Horizons: SU, 1cl Termination: Downlap	Seismic Horizons: 1cl' Termination: Toplap/ Erosion
	1a3		Amplitude: Low to medium Configuration: Chaotic/Transparent with internal reflections Geometry: Wedge/Mound	Seismic Horizons: 1cl, 1cl', SU, 2rw Termination: Downlap	Seismic Horizons: 1cl'' Termination: Toplap
	1c		Amplitude: Low Configuration: Transparent with some internal reflections Geometry: Sheet-like	Seismic Horizons: 2cl', 2rw, SU, 1cl, 1cl'' Termination: Downlap, Onlap	Seismic Horizons: 1sh Termination: Toplap
	1d		Amplitude: Low Configuration: Transparent with some internal reflections Geometry: Sheet-like	Seismic Horizons: 1cl'', 1sh Termination: Concordance	Seismic Horizons: 1rw Termination: Concordance/Erosion



Click here to access/download
Supplemental Material
fs_Carrion-Torrente.doc

